

De novo design of potent and selective mimics of IL-2 and IL-15

Daniel-Adriano Silva^{1,2,14*}, Shawn Yu^{1,3,14}, Umut Y. Ulge^{1,3,14}, Jamie B. Spangler^{4,5,14}, Kevin M. Jude⁵, Carlos Labão-Almeida⁶, Lestat R. Ali⁷, Alfredo Quijano-Rubio^{1,2,3}, Mikel Ruterbusch⁸, Isabel Leung⁹, Tamara Biary⁷, Stephanie J. Crowley⁷, Enrique Marcos^{1,2,10}, Carl D. Walkley^{1,2}, Brian D. Weitzner^{1,2}, Fátima Pardo-Avila¹¹, Javier Castellanos^{1,2}, Lauren Carter¹, Lance Stewart¹, Stanley R. Riddell⁹, Marion Pepper⁸, Gonçalo J. L. Bernardes^{6,12}, Michael Dougan⁷, K. Christopher Garcia^{5,13*} & David Baker^{1,2,13*}

We describe a de novo computational approach for designing proteins that recapitulate the binding sites of natural cytokines, but are otherwise unrelated in topology or amino acid sequence. We use this strategy to design mimics of the central immune cytokine interleukin-2 (IL-2) that bind to the IL-2 receptor $\beta\gamma_c$ heterodimer (IL-2R $\beta\gamma_c$) but have no binding site for IL-2R α (also called CD25) or IL-15R α (also known as CD215). The designs are hyper-stable, bind human and mouse IL-2R $\beta\gamma_c$ with higher affinity than the natural cytokines, and elicit downstream cell signalling independently of IL-2R α and IL-15R α . Crystal structures of the optimized design neoleukin-2/15 (Neo-2/15), both alone and in complex with IL-2R $\beta\gamma_c$, are very similar to the designed model. Neo-2/15 has superior therapeutic activity to IL-2 in mouse models of melanoma and colon cancer, with reduced toxicity and undetectable immunogenicity. Our strategy for building hyper-stable de novo mimetics could be applied generally to signalling proteins, enabling the creation of superior therapeutic candidates.

The considerable potential of the central immune cytokine interleukin-2 (IL-2) for cancer treatment^{1–3} has sparked numerous efforts to improve its therapeutic properties by mutation and/or chemical modification^{4–11}. Such efforts have sought to simplify manufacturing, extend half-life, and modulate interactions with receptors^{12–14}. However, there are inherent challenges to the development of a new therapeutic agent when starting with a naturally occurring bioactive protein. First, most natural proteins are only marginally stable^{15–17}; hence, amino acid substitutions aimed at increasing efficacy can decrease expression or cause aggregation, making manufacture and storage difficult. More substantial changes, such as deletion or fusion of functional or targeting domains, are often unworkable and can markedly alter pharmacokinetic properties and tissue penetration¹³. Second, any immune response against the engineered variant may cross-react with the endogenous molecule^{18–24} with potentially dangerous consequences. Third, the target receptor-subunit interaction profile can be difficult to reprogram. The clinical use of IL-2 has been mainly limited by toxicity^{25–27} which, although incompletely understood in humans, is considerably reduced in animals deficient in the IL-2R α chain (CD25 $^{-}$). Previous efforts to ablate the interaction between CD25 and IL-2 by either mutation^{5,8,28,29} (as in super-2) or PEGylation (for example, NKTR-214¹¹), have resulted in markedly reduced stability, binding, and/or potency of these reengineered cytokines, while failing to completely eliminate the interaction with CD25. Here we describe a computational design approach to generate mimetics of natural proteins with improved therapeutic properties that circumvent these challenges, allowing the engineering of hyper-stable de novo cytokine mimics that display specific receptor-binding interfaces that are optimal for treating disease.

IL-2/IL-15 mimics that bind and activate IL-2R $\beta\gamma_c$

Cytokines interact with multiple receptor subunits^{30–33}, and like most naturally occurring proteins, contain non-ideal structural features that compromise their stability but are important for function. We developed a computational protein design method in which the structural elements that interact with the desired receptor subunit(s) are fixed in space (Fig. 1a), and an idealized de novo globular protein structure is built to support these elements. De novo design has been used previously to support short linear epitopes^{34–37}; here we support more complex binding interfaces by using a parametric construction of disembodied helices coupled with knowledge-based loop closure³⁸ (Fig. 1b, c). We tested our approach by attempting de novo design of stable idealized proteins with interaction surfaces mimicking those of IL-2 and IL-15 for IL-2R $\beta\gamma_c$ ^{32,39}, but entirely lacking the CD25-interaction surface.

Native IL-2 comprises four helices (Fig. 1a) connected by long irregular loops. The N-terminal helix (H1) interacts with both the β - and γ -subunits, the third helix (H3) interacts with the β -subunit, and the C-terminal helix (H4) interacts with the γ -subunit. The α -subunit (CD25) interacting surface is formed by the irregular second helix (H2) and two long loops, one connecting H1 to H2 and the other connecting H3 to H4. We aimed to build an idealized protein that recapitulates the interface formed by H1, H3 and H4 with β and γ -subunits and to replace H2 with a helix that provides better packing and does not interact with the α -subunit. Two generations of designed mimics were made. In a first generation, we used all helices (H1, H2, H3 and H4) from IL-2 (Fig. 1a) as starting points for structure idealization by (independently) rebuilding each disembodied helix using commonly

¹Institute for Protein Design, University of Washington, Seattle, WA, USA. ²Department of Biochemistry, University of Washington, Seattle, WA, USA. ³Department of Bioengineering, University of Washington, Seattle, WA, USA. ⁴Departments of Biomedical Engineering and Chemical and Biomolecular Engineering, Johns Hopkins University, Baltimore, MD, USA. ⁵Departments of Molecular and Cellular Physiology and Structural Biology, Stanford University School of Medicine, Stanford, CA, USA. ⁶Instituto de Medicina Molecular, Faculdade de Medicina, Universidade de Lisboa, Lisbon, Portugal. ⁷Division of Gastroenterology, Massachusetts General Hospital, Harvard Medical School, Boston, MA, USA. ⁸Department of Immunology, University of Washington School of Medicine, Seattle, WA, USA. ⁹Fred Hutchinson Cancer Research Center, Clinical Research Division, Seattle, WA, USA. ¹⁰Institute for Research in Biomedicine (IRB Barcelona), The Barcelona Institute of Science and Technology, Barcelona, Spain. ¹¹Department of Structural Biology, Stanford University School of Medicine, Stanford, CA, USA. ¹²Department of Chemistry, University of Cambridge, Cambridge, UK. ¹³Howard Hughes Medical Institute, Chevy Chase, MD, USA. ¹⁴These authors contributed equally: Daniel-Adriano Silva, Shawn Yu, Umut Y. Ulge, Jamie B. Spangler.
*e-mail: dadriano@uw.edu; kcgarcia@stanford.edu; dabaker@uw.edu

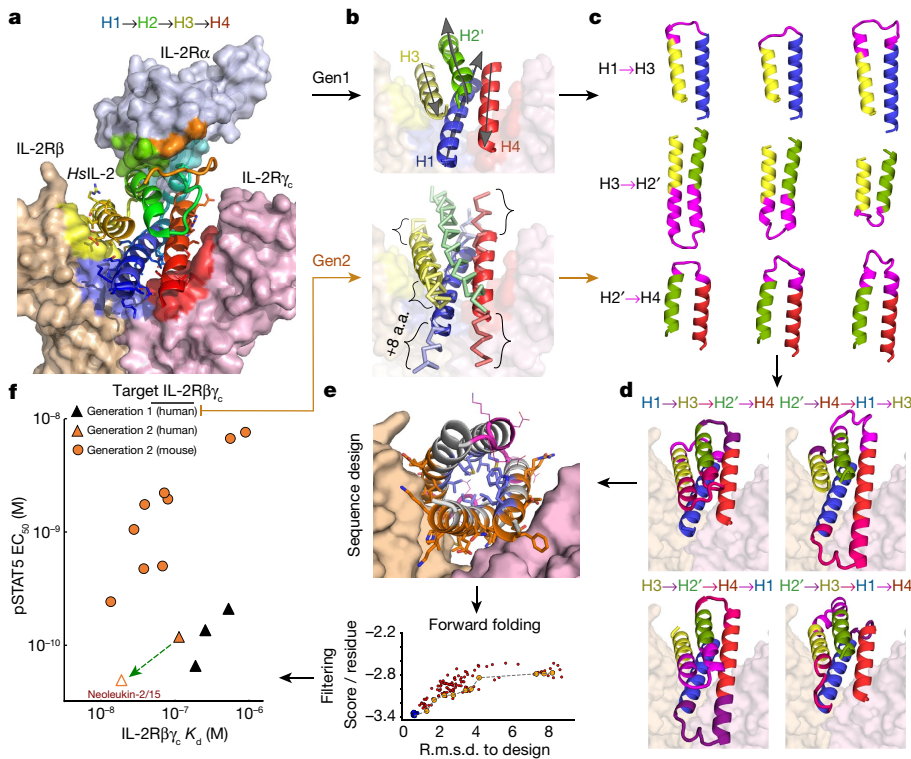


Fig. 1 | Computational design of de novo cytokine mimics. **a**, Structure of human IL-2 (HsIL-2) (cartoon representation) in complex with its receptor IL-2R $\alpha\beta\gamma_c$ (surface representation) (Protein Data Bank (PDB) ID: 2B5I). **b**, The designed mimics have four helices; three (blue, yellow and red) mimic IL-2 interactions with IL-2R $\beta\gamma_c$, whereas the fourth (green) holds the first three in place. Top, first generation (gen 1): each of the core elements of IL-2 (helices H1–H4) were independently idealized by assembly of four residue clustered protein fragments. Bottom, second generation (gen 2): the core elements were built using parametric

equations that recapitulate the shape of each disembodied helix, allowing changes in the length of each helix by up to ± 8 amino acids. **c**, Pairs of helices were reconnected using ideal loop fragments; representative examples are shown with the newly built elements connecting each pair of helices in magenta. **d**, Combination of helix hairpins in **c** to generate fully connected protein backbones. **e**, Rosetta flexible backbone sequence design. **f**, Binding and activity of selected designs (solid symbols), the green arrow originates at the parent of the best optimized design Neo-2/15 (see Extended Data Table 1).

occurring protein fragments (see Methods) and connecting helices with fragment-derived loops (Fig. 1c) to generate fully connected backbones (Fig. 1d). Rosetta combinatorial flexible backbone sequence design was carried out^{40–42} for each backbone (in complex with human IL-2R $\beta\gamma_c$), resulting in a considerably more regular structure for H2 (H2') than in IL-2 (Fig. 1b, top; see Methods). The four lowest-energy designs and eight single-disulfide-stapled variants (Supplementary Table 1) were selected for experimental characterization by yeast display (see Methods). Eight designs bound fluorescently-tagged $\beta\gamma$ -chimeric IL-2 receptor at low-nanomolar concentrations (Supplementary Fig. 1), and the highest affinity non-disulfide design (G1_neo2_40) was subjected to site-saturation mutagenesis (Supplementary Table 5) and selection for increased affinity to human IL-2R $\beta\gamma_c$. A second round of selection was then carried out on a library combining the best individual affinity-enhancing substitutions (combinatorial library, Supplementary Fig. 2, Supplementary Table 7). The highest-affinity variants (Supplementary Fig. 4, Supplementary Table 2) were expressed recombinantly in *Escherichia coli* and found to elicit pSTAT5 signalling in vitro on IL-2-responsive mouse cells at low-nanomolar or even picomolar concentrations (Extended Data Table 1), but had relatively low thermal stability (melting temperature, $T_m < 45^\circ\text{C}$, Supplementary Figs. 3, 5). To improve stability, in a second generation of designs, we repeated the computational design protocol starting from the backbone of the highest affinity first-round design (G1_neo2_40_1F, topology: H1→H4→H2'→H3), but this time coupling the loop-building process with parametric variation of the helix lengths (up to ± 8 amino acids, Fig. 1b, bottom). This second-generation approach improved the quality of the models by enabling the exploration of a substantially larger number of combinations of high-quality loops connecting each pair of helices. The 14 second-generation designs with highest predicted

affinity and stability, along with 27 Rosetta-sequence redesigns of G1_neo2_40_1F (Supplementary Table 3), were experimentally characterized. All but one of the designs were found to bind the human IL-2 receptor at low-nanomolar concentrations (Fig. 1f, Extended Data Table 1, Supplementary Fig. 6). The three designs with highest affinity and stability (one sequence redesign and two new mimetics) were subjected to site-saturation mutagenesis (Supplementary Table 6), followed by selection on combinatorial libraries of substitutions to increase affinity for mouse IL-2R $\beta\gamma_c$ (Supplementary Figs. 8–10, Supplementary Tables 6, 8), which yielded higher-affinity hyper-stable variants of the de novo mimics (Extended Data Table 1, Supplementary Tables 4, 8, Supplementary Figs. 11–13). The second-generation optimized design with highest overall affinity for both human and mouse IL-2R $\beta\gamma_c$, Neo-2/15, is a 100-residue protein with a topology and sequence that is quite different from human or mouse IL-2 (BLASTP sequence identity to human and mouse IL-2 of 14% and 24%, respectively; MICHAN structure-based sequence identity to human and mouse IL-2 of 29% and 16% respectively, see Methods and Extended Data Table 1).

Functional characterization of Neo-2/15

Neo-2/15 binds with high affinity to human and mouse IL-2R $\beta\gamma_c$ (with dissociation constants, $K_d \approx 19$ nM and $K_d \approx 38$ nM, respectively), but does not interact with IL-2R α (Fig. 2a). The affinities of Neo-2/15 for the human and mouse IL-2 receptors (IL-2R β and IL-2R $\beta\gamma_c$) are higher than those of the corresponding native IL-2 cytokines (Extended Data Table 1). Neo-2/15 activates IL-2R α^- human YT-1 cells more potently than native human IL-2 (half-maximal response dose, $EC_{50} = 49$ pM versus 410 pM for the native human IL-2). Similarly, Neo-2/15 activates IL-2R α^- mouse primary T cells more potently than native mouse

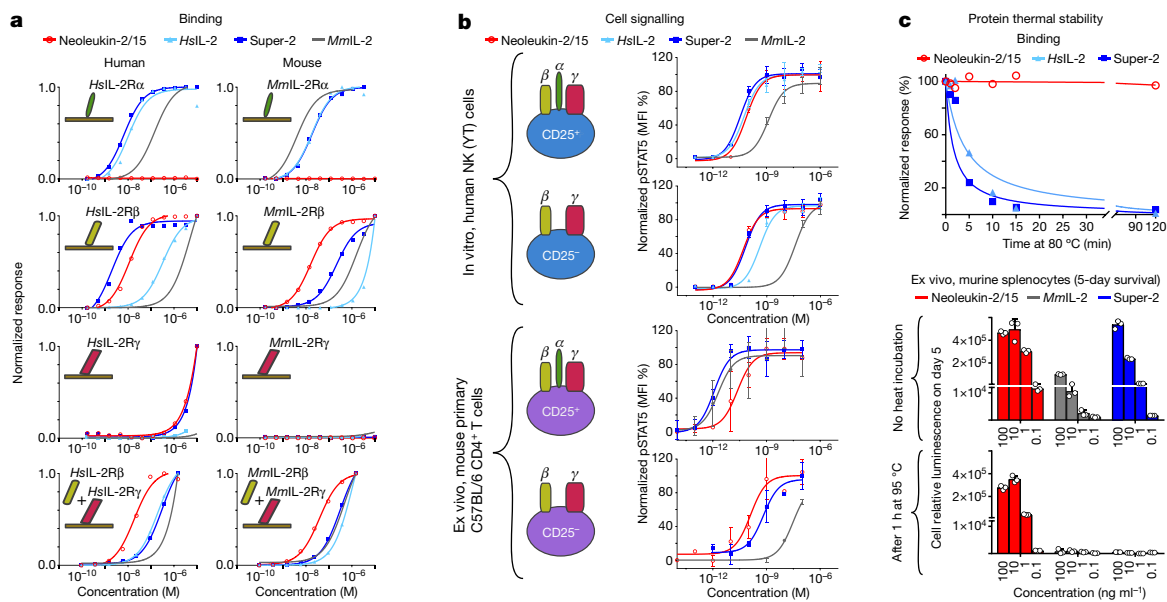


Fig. 2 | Characterization of Neo-2/15. **a**, Receptor subunit binding assessed by surface plasmon resonance (SPR). Neo-2/15 (red) does not bind IL-2R α (top row), but binds more tightly than IL-2 (light blue) and super-2 (dark blue) to IL-2R β (second row) and IL-2R $\beta\gamma_c$ (bottom row) (K_d values in Extended Data Table 1; experiments performed 3 times with similar results). **b**, Neo-2/15 stimulates STAT5 phosphorylation (pSTAT5) more potently than IL-2 in cells expressing IL-2R $\beta\gamma_c$ but lacking IL-2R α (CD25 $^-$) in both (in vitro) human NK cells (YT cell line; $n = 3$; experiments performed 3 times with similar results) and mouse primary

CD4 $^+$ T cells ($n = 4$; data from a pool of 3 independent experiments). **c**, Top, Neo-2/15 can be incubated for 2 h at 80 °C without loss of binding to human IL-2R $\beta\gamma_c$, whereas human IL-2 and super-2 quickly lose activity (immobilized IL-2R $\beta\gamma_c$ with soluble IL-2R β at 500 nM; experiment performed once). Bottom, following incubation at 95 °C for 1 h, Neo-2/15 still drives cell survival effectively (with ~70% luminescence remaining at 10 ng ml $^{-1}$ relative to cells treated with non-heat incubated neo 2/15), whereas mouse IL-2 (MmIL-2) and super-2 are inactivated ($n = 3$; experiment performed 3 times with similar results). Data are mean \pm s.d.

IL-2 ($EC_{50} = 130$ pM versus 30 nM). These results are consistent with the higher binding affinity of Neo-2/15 for the IL-2 receptors (Fig. 2b, Supplementary Table 9). Neo-2/15 is also more active than super-2, a variant of IL-2 engineered for higher affinity for IL-2R β^8 , on IL-2R α^- mouse primary T cells ($EC_{50} = 130$ pM versus 660 pM) and less active than super-2 on IL-2R α^+ cells ($EC_{50} = 24$ pM versus 1.2 pM), presumably owing to its complete lack of IL-2R α binding (Fig. 2b). Neo-2/15 is hyper-stable (Supplementary Fig. 13) and does not lose binding affinity for the IL-2R $\beta\gamma_c$ following incubation at 80 °C for 2 h, whereas human IL-2 and super-2 are inactivated after 10 min (half-inactivation time \approx 4.2 min and 2.6 min, respectively, Fig. 2c, top). In ex vivo primary cell cultures, Neo-2/15 drives T cell survival effectively after 60 min of boiling at 95 °C, whereas these conditions inactivated both IL-2 and super-2 (Fig. 2c, bottom). This unprecedented stability for a cytokine-like molecule, as well as elimination of the requirement for cold chain storage, suggests a robustness to mutations (Extended Data Fig. 8), genetic fusions, and chemical modification (Supplementary Fig. 14) greatly exceeding that of native IL-2, which could contribute to the development of improved or new therapeutic properties (Extended Data Figs. 3, 4).

Structure of Neo-2/15 and complex with MmIL-2R $\beta\gamma_c$

The X-ray crystal structure of Neo-2/15 is very similar to the computational design model (root mean square deviation of C α atoms, r.m.s.d. = 1.1–1.3 Å for the 6 copies in the asymmetric unit, Fig. 3a). We determined the structure of mouse IL-2R $\beta\gamma_c$ in complex with Neo-2/15 and found that it aligns very closely to the previously reported human IL-2 receptor complex 43 (Fig. 3b, Extended Data Table 2). The Neo-2/15 design model and the unbound crystal structure align with the mouse ternary complex structure with r.m.s.d. of 1.27 and 1.29 Å, respectively (Fig. 3c). The order of helices in Neo-2/15 (using IL-2 numbering) is H1 → H3 → H2' → H4 (Figs. 1a, 3a, d). The H1–H3 loop is disordered in the ternary complex, but helix H3 is in close agreement with the predicted structure; there is also an outward movement of helix H4 and the H2'–H4 loop compared to the monomeric structure (Fig. 3c). Neo-2/15 interacts with mouse IL-2R β via helices H1 and

H3, and with γ_c via the H1 and H4 helices (Fig. 3); these regions align closely with both the computational design model (Fig. 3a) and the monomeric crystal structure (Fig. 3c). A shift of about 4.0 Å for helix H4 (see Fig. 3c) in the mouse complex may reflect the optimization for high-affinity binding to both the mouse and human receptors. The design of Neo-2/15 was guided by the human complex structure, and simulations suggest that there is little or no helix shift in this complex (Extended Data Fig. 7). Consistent with this, the helices of apo Neo-2/15 superimpose closely on those of human IL-2 in complex with its receptor (Fig. 3e, f), despite the different topologies of the two proteins (Fig. 3d).

Therapeutic applications of Neo-2/15

The inherent low stability of IL-2 and its tightly evolved dependence on CD25 have been barriers to the clinical translation of re-engineered IL-2 compounds. Other efforts have focused on IL-15 44 , because it elicits similar signalling to IL-2 by dimerizing IL-2R $\beta\gamma_c$ but has no affinity for CD25. However, IL-15 activity is dependent on *trans* presentation of IL-15R α , which is displayed primarily on antigen-presenting cells and NK cells. The low stability of native IL-15 and its dependence on *trans* presentation have also presented substantial barriers to re-engineering efforts 44,45 .

Dose-escalation studies on naive mice show that Neo-2/15 causes lower expansion of immunosuppressive T regulatory (T $_{reg}$) cells than mouse IL-2 (Fig. 4a, left), leading to a higher CD8 $^+$ killer T cell:T $_{reg}$ ratio with Neo-2/15 (Fig. 4a, right). The increased expansion of T $_{reg}$ cells by mouse IL-2 is expected, because it binds preferentially to CD25 $^+$ cells 35,46,47 . The higher CD8 $^+$ T cell:T $_{reg}$ ratios achieved with Neo-2/15 are generally associated with better tumour killing 8,11,29 ; this functional advantage of Neo-2/15 is likely to stem from its higher affinity for IL-2R $\beta\gamma_c$ and lack of bias towards CD25 $^+$ cells. Similarly, in a mouse model of airway inflammation that normally induces a small percentage of tissue-resident CD8 $^+$ T cells (Thy1.2 $^-$ CD44 $^+$ CD8 $^+$), Neo-2/15 elicits an increase in the population of tissue-resident CD8 $^+$ T cells without increasing the population of antigen-specific T $_{reg}$ (CD4 $^+$ Foxp3 $^+$; Fig. 4b).

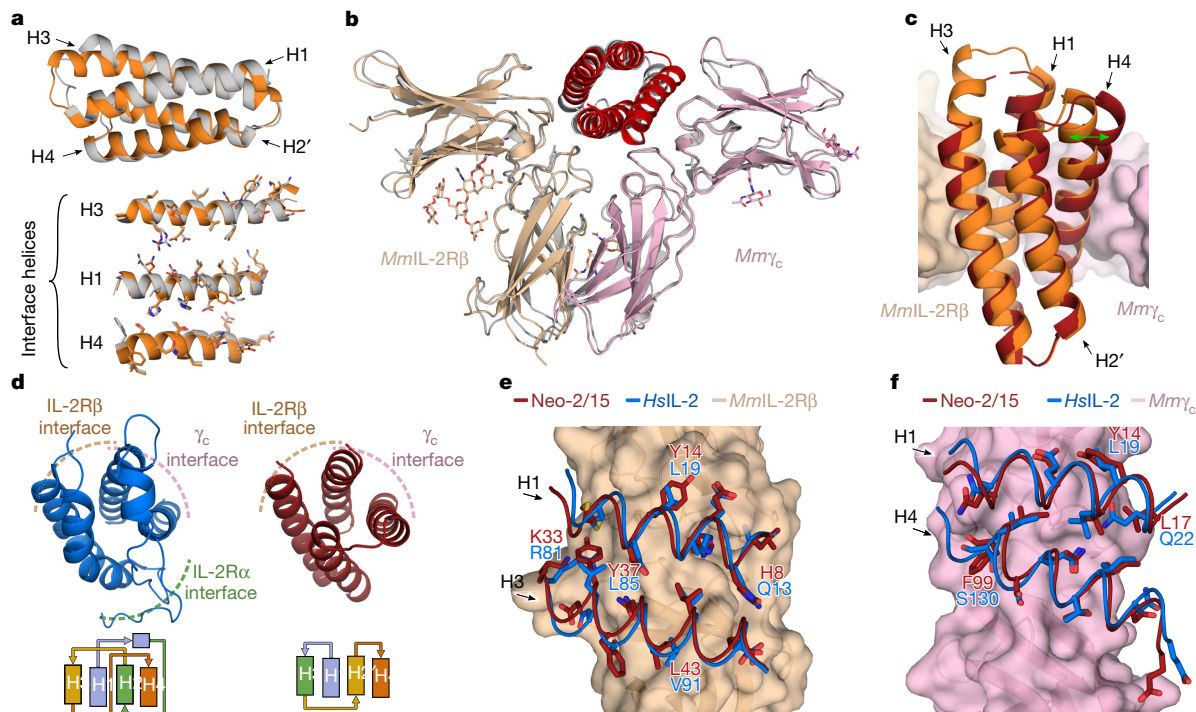


Fig. 3 | Structure of Neo-2/15 and its ternary complex with mouse IL-2R $\beta\gamma_c$. **a**, Top, structural alignment of Neo-2/15 chain A (orange) with the design model (grey, r.m.s.d. $\approx 1.11 \text{ \AA}$, for 100 C α atoms). Bottom, detail of interface helices H1, H3 and H4 (numbered according to *HsIL-2*, Fig. 1). The interface side chains are shown in sticks. **b**, Crystal structure of the ternary complex of Neo-2/15 (red) with mouse IL-2R β (wheat) and IL-2R γ_c (pink), aligned to the design model against human IL-2R $\beta\gamma_c$ (grey, r.m.s.d. $\approx 1.27 \text{ \AA}$, for the 93 modelled C α atoms of Neo-2/15 in the ternary complex). **c**, Structural alignment of monomeric Neo-2/15 (chain A, orange) with Neo-2/15 in the ternary complex (red, r.m.s.d. $\approx 1.71 \text{ \AA}$ for the 93 modelled C α atoms in the ternary complex), highlighting a

$\sim 4.0 \text{ \AA}$ shift of helix H4 in the ternary-complex structure compared to the monomeric crystal structure (green double-headed arrow). **d**, Comparison of the crystallographic structures of human IL-2 (cartoon representation in blue) (left) and Neo-2/15 from the ternary complex in **b** (cartoon representation in red) (right). The regions that interact with IL-2R β and γ_c are indicated. Topology diagrams are shown below the structures. The loop-rich region from IL-2 that interacts with the IL-2R α does not exist in the de novo mimic Neo-2/15. **e**, **f**, Comparison of the binding interfaces of Neo-2/15 and human IL-2. Interfacial amino acids are shown as sticks, and those that differ between human IL-2 and Neo-2/15 are denoted with labels.

To test whether Neo-2/15 is immunogenic, naïve and tumour-bearing mice were treated with Neo-2/15 daily (over a period of 4 weeks and 2 weeks, respectively). Little or no immunogenicity was observed in either case (Fig. 4c, Extended Data Fig. 5). A similar lack of immune response has been observed for other de novo-designed therapeutic candidates³⁵ (probably owing to their small size and high stability). Polyclonal antibodies against Neo-2/15 were generated by vaccinating mice with an inactive Neo-2/15 mutant—Neo-2/15(Y14D/F99D), also known as KO Neo-2/15—in complete Freund's adjuvant. These polyclonal Neo-2/15 antibodies do not cross-react with human or mouse IL-2 (Fig. 4c, Extended Data Fig. 5), suggesting that even if there is an immune response to Neo-2/15 in a therapeutic setting, this response is unlikely to cross-react with endogenous IL-2. This is consistent with the low sequence identity between Neo-2/15 and human or mouse IL-2 (Extended Data Table 1), which makes an autoimmune response against host IL-2 much less likely with Neo-2/15 than with previously engineered human IL-2 variants (for example, super-2 or PEGylated IL-2), which differ from endogenous IL-2 by only a few mutations (the BLASTP sequence identities of Neo-2/15 and super-2 to human IL-2 are 14% and 95%, respectively).

We tested the therapeutic efficacy of Neo-2/15 in B16F10 (melanoma) and CT26 (colon cancer) mouse models. Single-agent treatment with Neo-2/15 led to dose-dependent delays in tumour growth in both cancer models. In CT26 colon cancer, single-agent treatment showed improved efficacy compared to mouse IL-2 (Fig. 4d, Extended Data Fig. 1). In B16F10 melanoma, previous studies have shown that single-agent treatment with IL-2 is only partially effective, and co-treatment with the anti-melanoma cell antibody TA99 (anti-TRP1 monoclonal antibody) is synergistic with IL-2^{5,12,14} and IL-15 (superagonist complex ALT-803)⁴⁸. In long-term survival

experiments (8 weeks), Neo-2/15 in combination with TA99 showed substantially reduced toxicity and an overall superior therapeutic effect compared to mouse IL-2 (Fig. 4e, Extended Data Fig. 2), whereas treatment with TA99 alone had little effect. Mice treated with both mouse IL-2 and TA99 steadily lost weight and their overall health declined to the point of requiring euthanasia, whereas little decline was observed with the combination of Neo-2/15 and TA99 (Fig. 4e). Consistent with a therapeutic benefit, Neo-2/15 treatment led to significantly increased intratumoural CD8:T_{reg} ratios (Fig. 4f, Extended Data Fig. 1), which are known to correlate with effective antitumour immune responses⁴⁹. The increases of CD8:T_{reg} ratios with Neo-2/15 treatment are dose- and antigen-dependent (Fig. 4f), which is in agreement with the enhanced therapeutic effects observed at higher doses and in combination with TA99 (Extended Data Fig. 2). Collectively, these data show that Neo-2/15 exhibits the predicted homeostatic benefit derived from its IL-2-like immunostimulatory activity, but without the adverse effects associated with preferential binding to CD25⁺ cells. These enhanced properties and low toxicity could enable routine use of Neo-2/15 for indications for which IL-2 is not broadly used, such as to enhance CAR-T cell therapies (Extended Data Fig. 4). The activation of pSTAT5 signalling in naïve mouse peripheral blood lymphocytes (CD8⁺ T and B cells) observed an hour after exposure to Neo-2/15 was markedly reduced after three hours (Extended Data Fig. 6), suggesting that the efficacy of Neo-2/15 can be increased using standard approaches for extending circulation half-life, such as PEGylation⁵⁰.

De novo design of protein mimetics has the potential to transform the field of protein-based therapeutics, enabling the development of molecules that improve on biology by enhancing therapeutic properties and reducing side effects, not only for cytokines, but for almost

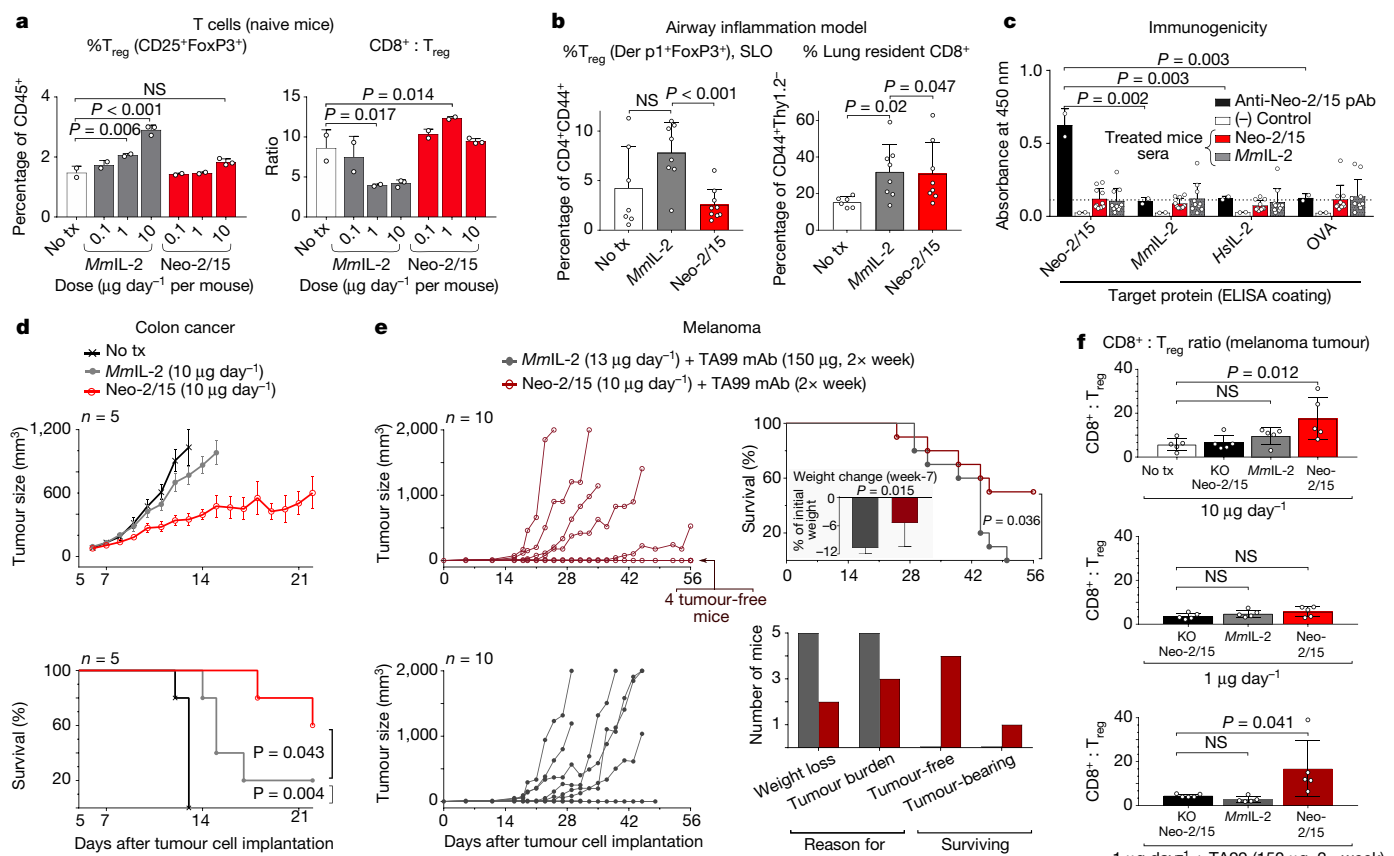


Fig. 4 | In vivo characterization of Neo-2/15. **a**, Mouse IL-2 but not Neo-2/15 enhances CD4⁺ T_{reg} expansion in naive mice T cells. *n* = 2 (no tx (no treatment); 0.1, 1 mouse IL-2; 0.1, 1 Neo-2/15); *n* = 3 (10 mouse IL-2; 10 Neo-2/15). **b**, In a mouse airway inflammation model (20 µg per day per mouse, 7 days), Neo-2/15 does not increase the frequency of antigen-specific CD4⁺Foxp3⁺ T_{reg} cells in the lymphoid organs (SLO). *n* = 6 (no tx); *n* = 8 (MmIL-2; Neo-2/15). **c**, Neo-2/15 does not have detectable immunogenicity. Mice were immunized with Neo-2/15 (red, *n* = 10) or mouse IL-2 (grey, *n* = 10) (14 days of daily intraperitoneal injections, 10 µg day⁻¹). IgG was detected by enzyme-linked immunosorbent assay (ELISA). Anti-Neo-2/15 polyclonal antibody was used as a positive control (black, *n* = 2) and did not cross-react with mouse or human IL-2. White, negative control (*n* = 2). OVA, ovalbumin. **d**, Neo-2/15 is more effective than mouse IL-2 in a colorectal cancer model (CT26). Starting on day 6, mice were administered daily with mouse IL-2 or Neo-2/15 (10 µg) intraperitoneally, or were left untreated. Top, tumour

any biologically active molecule with known or accurately predictable structure. Because of the incremental nature of current traditional engineering approaches (for example, 1–3 amino acid substitutions, chemical modification at a single site), most of the shortcomings of the parent molecule are inevitably passed on to the resulting engineered variants, often in an exacerbated form. By building mimics completely from scratch, these shortcomings can be avoided. Unlike recombinant IL-2 and its engineered variants, Neo-2/15 is highly expressed in *E. coli* (Supplementary Fig. 13), retains activity at high temperature, does not interact with IL-2R α , and is robust to substantial sequence changes (Extended Data Fig. 8), which may enable the engineering of new functions. Immunogenicity against the de novo designed proteins appears to be low, probably because of their small size and high stability³⁵, and in contrast to incremental variants of human IL-2, any antibody response mounted against mimetics is unlikely to cross-react with its natural (cytokine) counterpart. Because of their high stability and robustness, along with their tailored interaction surfaces, de novo designed protein mimetics are likely to be particularly powerful for developing next-generation therapeutics that combine different protein functionalities.

growth curves show only surviving mice and stop if a group fell below 50% of the initial *n*. Bottom, survival curves. Mice were euthanized if weight loss exceeded 10% or tumour size reached 1,000 mm³. **e**, In a melanoma model (B16F10), combination of mAb TA99 with Neo-2/15 is more effective than with mouse IL-2. Starting on day 1, mice were administered daily with Neo-2/15 (10 µg) or equimolar mouse IL-2 intraperitoneally. Twice-weekly treatment with TA99 was added on day 3. Left, tumour growth curves. Top right, survival curve; inset shows average weight change. Bottom right, quantification of the cause of death. **f**, Neo-2/15 elicits a higher CD8⁺:T_{reg} ratio than mouse IL-2. Data are mean \pm s.e.m. Results are analysed by one-way ANOVA (95% confidence interval), except survival curves, which are assessed using the Mantel–Cox test (95% confidence interval). All experiments were performed twice with similar results, except **b**, which shows data pooled from 3 independent experiments.

Online content

Any methods, additional references, Nature Research reporting summaries, source data, statements of data availability and associated accession codes are available at <https://doi.org/10.1038/s41586-018-0830-7>.

Received: 1 June 2018; Accepted: 15 November 2018;

Published online 9 January 2019.

- Akdis, M. et al. Interleukins, from 1 to 37, and interferon- γ ; receptors, functions, and roles in diseases. *J. Allergy Clin. Immunol.* **127**, 701–721 (2011).
- Smyth, M. J., Cretney, E., Kershaw, M. H. & Hayakawa, Y. Cytokines in cancer immunity and immunotherapy. *Immunol. Rev.* **202**, 275–293 (2004).
- Lotze, M. T. et al. In vivo administration of purified human interleukin 2. II. Half life, immunologic effects, and expansion of peripheral lymphoid cells in vivo with recombinant IL 2. *J. Immunol.* **135**, 2865–2875 (1985).
- Moraga, I. et al. Synthekines are surrogate cytokine and growth factor agonists that compel signalling through non-natural receptor dimers. *eLife* **6**, e22882 (2017).
- Vazquez-Lombardi, R. et al. Potent antitumour activity of interleukin-2-Fc fusion proteins requires Fc-mediated depletion of regulatory T-cells. *Nat. Commun.* **8**, 15373 (2017).
- Sockolosky, J. T. et al. Selective targeting of engineered T cells using orthogonal IL-2 cytokine–receptor complexes. *Science* **359**, 1037–1042 (2018).

7. Kureshi, R., Bahri, M. & Spangler, J. B. Reprogramming immune proteins as therapeutics using molecular engineering. *Curr. Opin. Chem. Eng.* **19**, 27–34 (2018).
8. Levin, A. M. et al. Exploiting a natural conformational switch to engineer an interleukin-2 ‘superkine’. *Nature* **484**, 529–533 (2012).
9. Sarkar, C. A. et al. Rational cytokine design for increased lifetime and enhanced potency using pH-activated ‘histidine switching’. *Nat. Biotechnol.* **20**, 908–913 (2002).
10. Spangler, J. B., Moraga, I., Mendoza, J. L. & Garcia, K. C. Insights into cytokine-receptor interactions from cytokine engineering. *Annu. Rev. Immunol.* **33**, 139–167 (2015).
11. Charych, D. H. et al. NKTR-214, an engineered cytokine with biased IL2 receptor binding, increased tumor exposure, and marked efficacy in mouse tumor models. *Clin. Cancer Res.* **22**, 680–690 (2016).
12. Dougan, M. et al. Targeting cytokine therapy to the pancreatic tumor microenvironment using PD-L1-specific VHHS. *Cancer Immunol. Res.* **6**, 389–401 (2018).
13. Tzeng, A., Kwan, B. H., Opel, C. F., Navaratna, T. & Dane Wittrup, K. Antigen specificity can be irrelevant to immunocytokine efficacy and biodistribution. *Proc. Natl Acad. Sci. USA* **112**, 3320–3325 (2015).
14. Zhu, E. F. et al. Synergistic innate and adaptive immune response to combination immunotherapy with anti-tumor antigen antibodies and extended serum half-life IL-2. *Cancer Cell* **27**, 489–501 (2015).
15. Kim, D. E., Gu, H. & Baker, D. The sequences of small proteins are not extensively optimized for rapid folding by natural selection. *Proc. Natl Acad. Sci. USA* **95**, 4982–4986 (1998).
16. Taverna, D. M. & Goldstein, R. A. Why are proteins marginally stable? *Proteins* **46**, 105–109 (2002).
17. Foit, L. et al. Optimizing protein stability in vivo. *Mol. Cell* **36**, 861–871 (2009).
18. Marshall, S. A., Lazar, G. A., Chirino, A. J. & Desjarlais, J. R. Rational design and engineering of therapeutic proteins. *Drug Discov. Today* **8**, 212–221 (2003).
19. De Groot, A. S. & Scott, D. W. Immunogenicity of protein therapeutics. *Trends Immunol.* **28**, 482–490 (2007).
20. Peyvandi, F. et al. A randomized trial of factor VIII and neutralizing antibodies in hemophilia A. *N. Engl. J. Med.* **374**, 2054–2064 (2016).
21. Antonelli, G., Currenti, M., Turriziani, O. & Dianzani, F. Neutralizing antibodies to interferon- α : relative frequency in patients treated with different interferon preparations. *J. Infect. Dis.* **163**, 882–885 (1991).
22. Eckardt, K.-U. & Casadevall, N. Pure red-cell aplasia due to anti-erythropoietin antibodies. *Nephrol. Dial. Transplant.* **18**, 865–869 (2003).
23. Prümmer, O. Treatment-induced antibodies to interleukin-2. *Biotherapy* **10**, 15–24 (1997).
24. Fineberg, S. E. et al. Immunological responses to exogenous insulin. *Endocr. Rev.* **28**, 625–652 (2007).
25. Boyman, O. & Sprent, J. The role of interleukin-2 during homeostasis and activation of the immune system. *Nat. Rev. Immunol.* **12**, 180–190 (2012).
26. Blattman, J. N. et al. Therapeutic use of IL-2 to enhance antiviral T-cell responses in vivo. *Nat. Med.* **9**, 540–547 (2003).
27. Siegel, J. P. & Puri, R. K. Interleukin-2 toxicity. *J. Clin. Oncol.* **9**, 694–704 (1991).
28. Mott, H. R. et al. The solution structure of the F42A mutant of human interleukin 2. *J. Mol. Biol.* **247**, 979–994 (1995).
29. Carmenante, T. et al. Human IL-2 mutant with higher antitumor efficacy than wild type IL-2. *J. Immunol.* **190**, 6230–6238 (2013).
30. Tagaya, Y., Bamford, R. N., DeFilippis, A. P. & Waldmann, T. A. IL-15: a pleiotropic cytokine with diverse receptor/signaling pathways whose expression is controlled at multiple levels. *Immunity* **4**, 329–336 (1996).
31. Ozaki, K. & Leonard, W. J. Cytokine and cytokine receptor pleiotropy and redundancy. *J. Biol. Chem.* **277**, 29355–29358 (2002).
32. Lin, J. X. et al. The role of shared receptor motifs and common Stat proteins in the generation of cytokine pleiotropy and redundancy by IL-2, IL-4, IL-7, IL-13, and IL-15. *Immunity* **2**, 331–339 (1995).
33. Ma, A., Boone, D. L. & Ladolce, J. P. The pleiotropic functions of interleukin 15: not so interleukin 2-like after all. *J. Exp. Med.* **191**, 753–756 (2000).
34. Procko, E. et al. A computationally designed inhibitor of an Epstein-Barr viral Bcl-2 protein induces apoptosis in infected cells. *Cell* **157**, 1644–1656 (2014).
35. Chevalier, A. et al. Massively parallel de novo protein design for targeted therapeutics. *Nature* **550**, 74–79 (2017).
36. Jacobs, T. M. et al. Design of structurally distinct proteins using strategies inspired by evolution. *Science* **352**, 687–690 (2016).
37. Correia, B. E. et al. Proof of principle for epitope-focused vaccine design. *Nature* **507**, 201–206 (2014).
38. Boyken, S. E. et al. De novo design of protein homo-oligomers with modular hydrogen-bond network-mediated specificity. *Science* **352**, 680–687 (2016).
39. Ring, A. M. et al. Mechanistic and structural insight into the functional dichotomy between IL-2 and IL-15. *Nat. Immunol.* **13**, 1187–1195 (2012).
40. Fleishman, S. J. et al. RosettaScripts: a scripting language interface to the Rosetta macromolecular modeling suite. *PLoS ONE* **6**, e20161 (2011).
41. Leaver-Fay, A. et al. Rosetta3: an object-oriented software suite for the simulation and design of macromolecules. *Methods Enzymol.* **487**, 545–574 (2011).
42. Chaudhury, S., Lyskov, S. & Gray, J. J. PyRosetta: a script-based interface for implementing molecular modeling algorithms using Rosetta. *Bioinformatics* **26**, 689–691 (2010).
43. Wang, X., Rickert, M. & Garcia, K. C. Structure of the quaternary complex of interleukin-2 with its α , β , and γ receptors. *Science* **310**, 1159–1163 (2005).
44. Robinson, T. O. & Schlunck, K. S. The potential and promise of IL-15 in immuno-oncogenic therapies. *Immunol. Lett.* **190**, 159–168 (2017).
45. Bouchaud, G. et al. The exon-3-encoded domain of IL-15R α contributes to IL-15 high-affinity binding and is crucial for the IL-15 antagonistic effect of soluble IL-15R α . *J. Mol. Biol.* **382**, 1–12 (2008).
46. Cao, X. Regulatory T cells and immune tolerance to tumors. *Immunol. Res.* **46**, 79–93 (2009).
47. Fontenot, J. D., Rasmussen, J. P., Gavin, M. A. & Rudensky, A. Y. A function for interleukin 2 in Foxp3-expressing regulatory T cells. *Nat. Immunol.* **6**, 1142–1151 (2005).
48. Chen, X. et al. Combination therapy of an IL-15 superagonist complex, ALT-803, and a tumor targeting monoclonal antibody promotes direct antitumor activity and protective vaccinal effect in a syngeneic mouse melanoma model. *J. Immunother. Cancer* **3**, 347 (2015).
49. Dougan, M. & Dranoff, G. Immune therapy for cancer. *Annu. Rev. Immunol.* **27**, 83–117 (2009).
50. Roberts, M. J., Bentley, M. D. & Harris, J. M. Chemistry for peptide and protein PEGylation. *Adv. Drug Deliv. Rev.* **64**, 116–127 (2012).

Acknowledgements We thank B. Nordstrom, J. Nordstrom, P. Barrier and J. Barrier for the IPD Fund (Budget Number: 68-0341); CONACyT SNI (Mexico), CONACyT postdoctoral fellowship (Mexico) and IPD translational research program to D.-A.S.; NIH MSTP grant T32 GM007266 to S.Y.; JDRF (2-SRA-2016-236-Q-R) to U.Y.U.; la Caixa Fellowship (la Caixa Banking Foundation, Barcelona, Spain) to A.Q.-R.; FCT Portugal Ph.D. studentship to C.L.-A.; European Research Council (ERC StG, grant agreement 676832), FCT Investigator (IF/00624/2015), and the Royal Society (UF110046 and URF/R180019) to G.J.L.B.; Marie Curie International Outgoing Fellowship (FP7-PEOPLE-2011-IOF 298976) to E.M.; Natural Sciences and Engineering Research Council of Canada Postdoctoral Fellowship to C.D.W.; Washington Research Foundation to B.D.W.; NIH grant R35GM122543 to F.P.-A.; Mentored Clinical Scientist Development Award 1K08DK114563-01, and the American Gastroenterological Association Research Scholars Award to M.D.; NIH-RO1-AI51321, NIH-RO1-AI51321, Mathers Foundation, Younger Endowed Chair, and Howard Hughes Medical Institute to K.C.G.; and Howard Hughes Medical Institute and Michelson Medical Research Foundation to D.B. See Supplementary Information for extended acknowledgements.

Reviewer information *Nature* thanks Y. Jones, W. Schief and the other anonymous reviewer(s) for their contribution to the peer review of this work.

Author contributions D.-A.S., S.Y., U.Y.U., J.B.S., M.P., G.J.L.B., M.D., K.C.G. and D.B. designed the research; D.-A.S. developed the method for designing de novo protein mimics, and designed and invented the IL-2/IL-15 mimics; S.Y., D.-A.S. and U.Y.U. characterized and optimized the IL-2/IL-15 mimics; J.B.S. performed BLI binding characterization, in vitro cell signalling, and recombinant IL-receptor production; K.M.J. performed crystallography experiments; A.Q.-R. characterized binding and stability, directed evolution and protein expression; L.R.A., T.B. and S.J.C. performed in vivo naïve mouse T cell response, melanoma cancer model and immunogenicity experiments; C.L.-A. performed in vivo colorectal cancer experiments; M.R. performed ex vivo cell signalling and in vivo airway inflammation experiments; I.L. performed in vivo CAR-T cell experiments; C.D.W. designed and characterized single-cysteine mutations; E.M. and J.C. assisted in developing the computational design methods; B.D.W. designed and characterized disulfide-stapled variants; F.P.-A. performed and analysed molecular dynamics simulations; L.C. performed optimization and production of recombinant protein; L.S. supervised and coordinated collaborations; S.R.R. supervised in vivo CAR-T cell experiments, M.P. supervised research for ex vivo cell signalling and in vivo tissue residency; G.J.L.B. supervised research for the in vivo colorectal cancer model; M.D. coordinated research for in vivo naïve mouse T cell response, melanoma cancer model and immunogenicity; D.-A.S., S.Y., U.Y.U., J.B.S., M.D., K.C.G. and D.B. wrote the manuscript; D.-A.S., K.C.G. and D.B. supervised and coordinated the overall research.

Competing interests D.-A.S., S.Y., U.Y.U., A.Q.-R., C.D.W. and D.B. are co-founders and stockholders of Neoleukin Therapeutics, a company that aims to develop the inventions described in this manuscript. D.-A.S., S.Y., U.Y.U., J.B.S., A.Q.-R., K.C.G. and D.B. are co-inventors on a US provisional patent application (no. 62/689769), which incorporates discoveries described in this manuscript.

Additional information

Extended data is available for this paper at <https://doi.org/10.1038/s41586-018-0830-7>.

Supplementary information is available for this paper at <https://doi.org/10.1038/s41586-018-0830-7>.

Reprints and permissions information is available at <http://www.nature.com/reprints>.

Correspondence and requests for materials should be addressed to D.-A.S. or K.C.G. or D.B.

Publisher's note: Springer Nature remains neutral with regard to jurisdictional claims in published maps and institutional affiliations.

METHODS

No statistical methods were used to predetermine sample size. The experiments were not randomized. The investigators were not blinded to allocation during experiments and outcome assessment.

Computational design of de novo cytokine mimetics. The design of de novo cytokine mimetics began by defining the structure of human IL-2 in the quaternary complex with the human IL-2R $\beta\gamma_c$ receptor as the template for the design. After inspection, the residues composing the binding site were defined as hotspots. The structure was fed into the new mimetic design protocol that is programmed in PyRosetta, which can automatically detect the core secondary structure elements that compose the target template and produce the resulting de novo mimetic backbones. In brief, the mimetic building algorithm works as follows. For the first generation of designs, each of the core elements was idealized by reconstruction using loops from a clustered database of highly ideal fragments (fragment size = 4 amino acids, see Data availability). After idealization, the mimetic building protocol aims to reconnect the idealized elements by pairs in all possible combinations. To do this, it uses combinatorial fragment assembly of sequence-agnostic fragments from the database, followed by Cartesian-constrained backbone minimization for potential solutions (that is, where the N and C ends of the built fragment are close enough to link the two secondary structures). After minimization, the solutions are verified to contain highly ideal fragments (that is, that every overlapping fragment that composes the two connected elements is also contained within the database) and that no backbone clashes with the target (context) receptor. Successful solutions were then profiled using the same database of fragments in order to determine the most probable amino acids at each position (this information was encoded as metadata on each design). Next, solutions for pairs of connected secondary structures were combinatorially recombined (by using graph theory-connected components) to produce fully connected backbones. Since the number of solutions grows exponentially with each pair of elements, at each fragment combination step we ranked the designs to favour those with shorter interconnections between pairs of secondary structure core elements (that is, effectively with shorter loops), and kept only the top solutions. Fully connected backbone solutions were profiled by layer (interface, core, non-core surface, surface) in order to restrict the identities of the possible amino acids to be layer-compatible. Finally, all the information on hotspots, compatible built-fragment amino acids and layers was combined (hotspot has precedence to amino acid probability, and amino acid probability took precedence to layer) and output as Rosetta resfiles (specific for a given de novo mimic backbone result). These backbones and their corresponding resfiles were then passed to RosettaScripts for flexible backbone design and filtering (Supplementary Information, Appendix A). For the second generation of designs, we followed two approaches. In the first approach, we simply executed Rosetta sequence redesigns of our best first generation optimized design (G1_neo2_40_1F, Supplementary Information, Appendix B). In the second approach, we engineered new mimetics using G1_neo2_40_1F as the target template. The mimetic design protocol in this second generation was similar to the one described for the first generation, but with two key differences. First, the core elements (that is, those that are secondary structures) were no longer built from fragments, but instead by discovering parametric equations of repetitive phi and psi angles (omega fixed to 180°) that result in secondary structures that recapitulated each of the target helices as close as possible. Second, a 'pitch' on the phi and psi angles was allowed every 3rd residue in order to allow the helices the possibility to have curvature (final angle parameters: H1: phi = -60.4, psi = -45.8, phi_pitch = -1.0, psi_pitch = 2.0; H2: phi = -64.5, psi = -38.4, phi_pitch = 4.0, psi_pitch = -8.0; H3: phi = -64.6, psi = -40.6, phi_pitch = 0.0, psi_pitch = 0.0; H4: phi = -64.3, psi = -41.7, phi_pitch = 0.0, psi_pitch = 0.0). By using these parametric equations, the algorithm can variate the length of each of the core-elements up to ± 8 amino acids (compared to the input template). Reductions in the size of the core elements were not allowed to remove hotspots from the binding site. All length variations of the core elements were reconnected with loops from a clustered database of highly ideal loops (fragment size of 7 amino acids). The rest of the design algorithm is in essence similar to the one followed in the generation one. However, the implementation of the second generation algorithm is more convenient, because the input PDB incorporates PDBInfoLabels metadata to define the hotspots, and subsequently, it uses this information to integrate the loop amino acids-preferences, layers, and hotspots into the final output(s) as PDBInfoLabels metadata. This information can be conveniently used for the subsequent step of sequence design with RosettaScripts (Supplementary Information, Appendix C). The Rosetta energy functions used for sequence design were 'talaris2013' and 'talaris2014', for the first and second generation of designs, respectively.

The databases of highly ideal fragments used for the design of the backbones for the de novo mimetics were constructed with the Rosetta application 'kccenters_clustering_of_fragments' using an extensive database of non-redundant (publicly available) protein structures from the RCSB protein data bank, which was comprised of 16,767 PDB structures for the 4-mer database used in the first

generation of designs, and of 7,062 PDB structures for the 7-mer database used for the second generation designs (see Code availability). The computational algorithm for designing the second generation de novo mimics is available (see Code availability).

Yeast display. Yeast were transformed with genes encoding the proteins to be displayed together with a linearized pETcon3 vector. The vector was linearized by 100-fold overdigestion by NdeI and XbaI (New England Biolabs) and then purified by gel extraction (Qiagen). The genes included 50 bases of overlap with the vector on both the 5' and 3' ends, such that homologous recombination would place the genes in frame between the AGA2 gene and the Myc tag on the vector. Yeast was grown in C-Trp-Ura medium before induction in SGCAA medium as previously described^{34,35,51}. After induction for 12–18 h, cells were washed in chilled display buffer (50 mM NaPO₄ pH 8, 20 mM NaCl, 0.5% BSA) and incubated with varying concentrations of biotinylated receptor (either human or mouse IL-2R α , IL-2R β or γ_c) while being agitated at 4°C. After approximately 30 min, cells were washed again in a chilled buffer and then incubated on ice for 5 min with a FITC-conjugated Myc antibody (1 μ l per 3 \times 10⁶ cells) and streptavidin-phycocerythrin (1 μ l per 100 μ l volume of yeast). Yeast was then washed and counted by flow cytometry (Accuri C6) or sorted by fluorescence-activated cell sorting (FACS) (Sony SH8000).

Mutagenesis and affinity maturation. Site-saturation mutagenesis (SSM) libraries were constructed from synthetic DNA from Genscript. For each amino acid on each design template, forward primers and reverse primers were designed such that PCR amplification would result in a 5' PCR product with a degenerate NNK codon and a 3' PCR product, respectively. Amplification of 'left' and 'right' products by COF and COR primers yielded a series of template products each consisting of a degenerate NNK codon at a different residue position. For each design, these products were pooled to yield the SSM library. SSM libraries were transformed by electroporation into conditioned *Saccharomyces cerevisiae* strain EBY100 cells, along with linearized pETcon3 vector, using the previously described protocol⁵². For details of the primers used in the creation of SSM libraries, see Supplementary Tables 5, 6.

Combinatorial libraries were constructed from synthetic DNA from Genscript containing ambiguous nucleotides and similarly transformed into a linearized pETcon3 vector. For details of the primers used in the creation of combinatorial libraries see Supplementary Tables 7, 8.

Protein expression. Genes encoding the designed protein sequences were synthesized and cloned into pET-28b(+) *E. coli* plasmid expression vectors (GenScript, N-terminal 6x His-tagged followed by a thrombin cleavage site. For all the designed proteins, the sequence of the N-terminal tag used is MGSSHHHHHSSGLVPRGSHM (unless otherwise noted), which is followed immediately by the sequence of the designed protein. Plasmids were then transformed into chemically competent *E. coli* Lemo21 cells (NEB). Protein expression was performed using terrific broth and M salts, cultures were grown at 37°C until $A_{600\text{ nm}}$ reached approximately 0.8, then expression was induced with 1 mM isopropyl β -D-thiogalactopyranoside (IPTG), and the temperature was lowered to 18°C. After expression for approximately 18 h, cells were harvested and lysed with a Microfluidics M110P microfluidizer at 18,000 psi, then the soluble fraction was clarified by centrifugation at 24,000g for 20 min. The soluble fraction was purified by Immobilized Metal Affinity Chromatography (Qiagen) followed by FPLC size-exclusion chromatography (Superdex 75 10/300 GL, GE Healthcare). The purified Neo-2/15 was characterized by mass spectrum verification of the molecular weight of the species in solution (Thermo Scientific), size-exclusion chromatography-multi-angle laser light scattering (SEC-MALLS) in order to verify monomeric state and molecular weight (Agilent, Wyatt), SDS-PAGE, and endotoxin levels (Charles River).

Human and mouse IL-2 complex components including human IL-2 (residues 1–133), human IL-2R α (residues 1–217), human IL-2R β (residues 1–214), human IL-2R γ_c (residues 1–232), mouse IL-2 (residues 1–149), mouse IL-2R α ectodomain (residues 1–213), mouse IL-2R β ectodomain (residues 1–215), and mouse γ_c ectodomain (residues 1–233) were secreted and purified using a baculovirus expression system, as previously described^{39,43}. For the zipped human IL-2R $\beta\gamma_c$ heterodimer, the aforementioned extracellular domain residues for the human/mouse IL-2R β and human/mouse IL-2R γ_c were separately cloned into baculovirus expression constructs containing 3C protease-cleavable basic and acidic leucine zippers, respectively, for a high-fidelity pairing of the receptor subunits, as described previously⁵³. The IL-2R β and IL-2R γ_c constructs were transfected independently and their corresponding viruses were co-titrated to determine optimal infection ratios for equivalent expression of the two chains. Insect cell secretion and purification proceeded as described for IL-2 cytokine and receptor subunits. All proteins were purified to >98% homogeneity with a Superdex 200 sizing column (GE Healthcare) equilibrated in Hepes-buffered saline (HBS). Purity was verified by SDS-PAGE analysis. For expression of biotinylated human IL-2 and mouse IL-2 receptor subunits, proteins containing a C-terminal biotin acceptor

peptide (BAP, LNDIFEAQKIEWHE) were expressed and purified as described by Ni-NTA affinity chromatography and then biotinylated with the soluble BirA ligase enzyme in 0.5 mM bicine pH 8.3, 100 mM ATP, 100 mM magnesium acetate, and 500 mM biotin (Sigma). Excess biotin was removed by size-exclusion chromatography on a Superdex 200 column equilibrated in HBS.

Neo-2/15 crystal and co-crystal structures. C-terminally 6× His-tagged endoglycosidase H (endoH) and mouse IL-2R β and IL-2R γ_c were expressed separately in High Five cells using a baculovirus system as previously described⁵². Cells expressing IL-2R γ_c were grown in the presence of 5 μ M kifunensine. After approximately 72 h, the secreted proteins were purified from the medium by passing over a Ni-NTA agarose column and eluted with 200 mM imidazole in HBS buffer (150 mM NaCl, 10 mM HEPES pH 7.3). EndoH was exchanged into HBS buffer by diafiltration. Mouse IL-2R γ_c was deglycosylated by overnight incubation with 1:75 (w/w) endoH. Mouse IL-2R β and IL-2R γ_c were further purified and buffer was exchanged by FPLC using an S200 column (GE Life Sciences).

Monomeric Neo-2/15 was concentrated to 12 mg/ml and crystallized by vapour diffusion from 2.4 M sodium malonate pH 7.0, and crystals were harvested and flash frozen without further cryoprotection. Crystals diffracted to 2.0 Å resolution at Stanford Synchrotron Radiation Laboratory beamline 12-2 and were indexed and integrated using XDS⁵⁴. The space group was assigned with Pointless⁵⁵, and scaling was performed with Aimless⁵⁶ from the CCP4 suite⁵⁷. Our predicted model was used as a search ensemble to solve the structure by molecular replacement in Phaser⁵⁸, with six protomers located in the asymmetric unit. After initial rebuilding with Autobuild⁵⁹, iterative cycles of manual rebuilding and refinement were performed using Coot⁶⁰ and PHENIX⁶¹.

To crystallize the ternary Neo-2/15-mouse IL-2R β -mouse IL-2R γ_c complex, the three proteins were combined in equimolar ratios, digested overnight with 1:100 (w/w) carboxypeptidases A and B to remove purification tags, and purified by FPLC using an S200 column; fractions containing all three proteins were pooled and concentrated to 20 mg/ml. Initial needle-like microcrystals were formed by vapour diffusion from 0.1 M imidazole pH 8.0, 1 M sodium citrate and used to prepare a microseed stock for subsequent use in microseed matrix screening⁶² (MMS). After a single iteration of MMS, crystals grown in the same precipitant were cryoprotected with 30% ethylene glycol, harvested and diffracted anisotropically to 3.4 Å × 3.8 Å × 4.1 Å resolution at Advanced Photon Source beamline 23ID-B. The structure was solved by molecular replacement in Phaser using the human IL-2R β and IL-2R γ_c structures (PDB ID: 2B51) as search ensembles. This produced an electron density map into which two poly-alanine α -helices could be manually built. Following rigid-body refinement in PHENIX, electron density for the two unmodelled alpha helices, along with the BC loop and some aromatic side chains, became visible, allowing docking of the monomeric Neo-2/15. Two further iterations of MMS and use of an additive screen (Hampton Research) produced crystals grown by vapour diffusion using 150 nl protein, 125 nl well solution containing 0.1 M Tris pH 7.5, 5% dextran sulfate, 2.1 M ammonium sulfate and 25 nl microseed stock containing 1.3 M ammonium sulfate, 50 mM Tris pH 7.5, 50 mM imidazole pH 8.0, 300 mM sodium citrate. Crystals cryoprotected with 3 M sodium malonate were flash frozen and diffracted anisotropically to 2.5 Å × 3.7 Å × 3.8 Å at Advanced Light Source beamline 5.0.1. After processing the data with XDS, an elliptical resolution limit was applied using the STARANISO server (<http://staraniso.globalphasing.org/>) as described⁶³. Rapid convergence of the model was obtained by refinement against these reflections using TLS and target restraints to the higher resolution human receptor (PDB ID: 2B51) and Neo-2/15 structures in Buster v.2.10.3⁶⁴, with manual rebuilding in Coot, followed by a final round of refinement in PHENIX with no target restraints. Structure figures were prepared with PyMOL⁶⁵. Software used in this project was installed and configured by SBGrid⁶⁶.

Cell lines. Unmodified YT-1⁶⁷ and IL-2R α^+ YT-1 human NK cells⁶⁸ were cultured in RPMI complete medium (RPMI 1640 medium supplemented with 10% fetal bovine serum (FBS), 2 mM L-glutamine, minimum non-essential amino acids, sodium pyruvate, 25 mM HEPES, and penicillin-streptomycin (Gibco)). CTLL-2 cells purchased from ATCC were cultured in RPMI complete with 10% T-STIM culture supplement with ConA (Corning). Twenty-four hours before signalling studies, CTLL-2 cells were resuspended in RPMI lacking T-STIM culture supplement for IL-2 starvation. Viability (>95%) of CTLL-2 cells was verified by trypan blue exclusion (counted in a haemocytometer) immediately before performing the signalling assays. All cells were maintained at 37 °C in a humidified atmosphere with 5% CO₂. The subpopulation of YT-1 cells expressing IL-2R α was purified via magnetic selection as described previously³⁹. Enrichment and persistence of IL-2R α expression were monitored by analysis of phycoerythrin (PE)-conjugated anti-human IL-2R α (BioLegend) antibody binding on an Accuri C6 flow cytometer (BD Biosciences). Cell lines were regularly tested via PCR to ensure the absence of mycoplasma contamination.

Circular dichroism. Far-ultraviolet circular dichroism measurements were carried out with an AVIV spectrometer model 420 in PBS (pH 7.4) in a 1 mm path length

cuvette with a protein concentration of ~0.20 mg/ml (unless otherwise mentioned in the text). Temperature melts were performed from 25 to 95 °C and monitored absorption signal at 222 nm (steps of 2 °C/min, 30 s of equilibration by step). Wavelength scans (195–260 nm) were collected at 25 °C and 95 °C, and again at 25 °C after fast refolding (~5 min).

Binding studies. Surface plasmon resonance (SPR): For IL-2 receptor affinity titration studies, biotinylated human or mouse IL-2R α , IL-2R β , and IL-2R γ_c receptors were immobilized to streptavidin-coated chips for analysis on a Biacore T100 instrument (GE Healthcare). An irrelevant biotinylated protein was immobilized in the reference channel to subtract non-specific binding. Less than 100 response units (RU) of each ligand was immobilized to minimize mass transfer effects. Threefold serial dilutions of human IL-2, mouse IL-2, super-2, or engineered IL-2 mimetics, were flowed over the immobilized ligands for 60 s and dissociation was measured for 240 s. For IL-2R β binding studies, saturating concentrations of human IL-2R β (3 μ M) or mouse IL-2R β (5 μ M) were added to the indicated concentrations of human IL-2 or mouse IL-2, respectively. Surface regeneration for all interactions was conducted using 15 s exposure to 1 M MgCl₂ in 10 mM sodium acetate pH 5.5. SPR experiments were carried out in HBS-P+ buffer (GE Healthcare) supplemented with 0.2% bovine serum albumin (BSA) at 25 °C, and all binding studies were performed at a flow rate of 50 l min⁻¹ to prevent analyte rebinding. Data was visualized and processed using the Biacore T100 evaluation software version 2.0 (GE Healthcare). Equilibrium titration curve fitting and equilibrium binding dissociation (K_d) value determination was implemented using GraphPad Prism assuming all binding interactions to be first order. SPR experiments were reproduced three times with similar results. Biolayer interferometry: binding data were collected in a Octet RED96 (ForteBio) and processed using the instrument's integrated software using a 1:1 binding model. Biotinylated target receptors, either human or mouse IL-2R α , IL-2R β or γ_c were functionalized to streptavidin-coated biosensors (SA ForteBio) at 1 μ g/ml in binding buffer (10 mM HEPES (pH 7.4), 150 mM NaCl, 3 mM EDTA, 0.05% surfactant P20, 0.5% non-fat dry milk) for 300 s. Analyte proteins were diluted from concentrated stocks into binding buffer. After baseline measurement in binding buffer alone, the binding kinetics were monitored by dipping the biosensors in wells containing the target protein at the indicated concentration (association step) and then dipping the sensors back into baseline/buffer (dissociation). For heterodimeric receptor binding experiments for IL-2R β - γ_c was bound to the sensor while IL-2R β was in solution at saturating concentrations (that is, at least ~2.5 fold molar excess over the K_d).

STAT5 phosphorylation studies. In vitro studies: Approximately 2×10^5 YT-1, IL-2R α^+ YT-1, or starved CTLL-2 cells were plated in each well of a 96-well plate and re-suspended in RPMI complete medium containing serial dilutions of human IL-2, mouse IL-2, super-2, or engineered IL-2 mimetics. Cells were stimulated for 15 min at 37 °C and immediately fixed by addition of formaldehyde to 1.5% and 10 min incubation at room temperature. Permeabilization of cells was achieved by resuspension in ice-cold 100% methanol for 30 min at 4 °C. Fixed and permeabilized cells were washed twice with FACS buffer (PBS pH 7.2 containing 0.1% bovine serum albumin) and incubated with Alexa Fluor 647-conjugated anti-STAT5 pY694 (BD Biosciences) diluted 1:50 in FACS buffer for 2 h at room temperature. Cells were then washed twice in FACS buffer and mean fluorescence intensity (MFI) was determined on a CytoFLEX flow cytometer (Beckman-Coulter). Dose-response curves were fitted to a logistic model and half-maximal effective concentration (EC₅₀ values) and corresponding 95% confidence intervals were calculated using GraphPad Prism data analysis software after subtraction of the MFI of unstimulated cells and normalization to the maximum signal intensity. Ex vivo studies: spleens and lymph nodes were collected from wild-type C57BL/6J or B6;129S4-Il2ra^{m1Dw} (CD25KO) mice purchased from The Jackson Laboratory and made into a single cell suspension in sort buffer (2% fetal calf serum in PBS pH 7.2). CD4 $^+$ T cells were enriched through negative selection by staining the cell suspension with biotin-conjugated anti-B220, CD8, NK1.1, CD11b, CD11c, Ter119, and CD19 antibodies at 1:100 for 30 min on ice. Following a wash with sort buffer, anti-biotin MicroBeads (Miltenyi Biotec) were added to the cell suspension at 20 μ l per 10^7 total cells and incubated on ice for 20 min. Cells were washed and then resuspended. Negative selection was then performed using EasySep Magnets (STEMCELL Technologies). Approximately 1×10^5 enriched cells were added to each well of a 96-well plate in RPMI complete medium with 5% FCS with tenfold serial dilutions of mouse IL-2, super-2, or Neo-2/15. Cells were stimulated for 20 min at 37 °C in 5% CO₂, fixed with 4% PFA and incubated for 30 min at 4 °C. Following fixation, cells were harvested and washed twice with sort buffer and again fixed in 500 μ l 90% ice-cold methanol in dH₂O for 30 min on ice for permeabilization. Cells were washed twice with Perm/Wash Buffer (BD Biosciences) and stained with anti-CD4-PerCP in Perm/Wash buffer (1:300), anti-CD44-Alexa Fluor 700 (1:200), anti-CD25-PE-Cy7 (1:200), and 5 μ l per sample of anti-pSTAT5-PE pY694 for 45 min at room temperature in the dark. Cells were washed with Perm/Wash and re-suspended in sort buffer for analysis

on a BD LSR II flow cytometer (BD Biosciences). Dose-response curves were fitted to a logistic model and EC₅₀ values and corresponding 95% confidence intervals were determined using GraphPad Prism data analysis software after subtraction of the MFI of untreated cells and normalization to the maximum signal intensity. Experiments were performed in triplicate and repeated three times with similar results.

In vivo mouse airway inflammation experiments. Mice (C57BL/6J, The Jackson Laboratory) were inoculated intranasally with 20 µl whole house dust mite antigen (Greer) resuspended in PBS to a total of 23 µg Derp1 per mouse. From days 1–7, mice were given a daily intraperitoneal injection of 20 µg mouse IL-2 in sterile PBS (pH 7.2), a molar equivalent of Neo-2/15 in sterile PBS, or no injection. On Day 8, circulating T cells were intravascularly labelled and tetramer-positive cells were enriched from lymph nodes and spleen or lung as previously described⁶⁹. Both the column flow-through and bound fractions were saved for flow cytometry analysis. Cells were surface stained with antibodies and analysed on a BD LSR II flow cytometer with BD FACSDiva software (BD Biosciences). Antibodies used: FITC anti-Ki67, clone SolA15, PerCP-Cy5.5 anti-CD25, clone PC61, eFluor 450 anti-Foxp3, clone FJK-16S, BV510 anti-CD8, clone 53-6.7, BV605 anti-PD-1, clone J43, BV711 anti-CD4, clone RM4-5, BV786 anti-CD62L, clone MEL-14, PE anti-CD69, clone H1.2F3, PE-CF594 anti-B220, clone RA3-6B2, PE-Cy7 anti-CXCR5, clone 2G8 and BUV395 anti-Thy1.2, clone 53-2.1. All flow cytometry files were analysed using FlowJo 9.9.4 and statistical analysis was performed using Prism 7. All experiments were performed in accordance with the University of Washington Institutional Care and Use Committee guidelines.

Colorectal carcinoma in vivo mice experiments. CT26 cells were sourced from the research group of J. Demenegeot at Instituto Gulbenkian de Ciéncia, Portugal. On day 0, 5×10^5 cells were injected subcutaneously into the flanks of BALB/c mice purchased from Charles River with 50 µl of a 1:1 mixture of Dulbecco's modified Eagle medium (Gibco) with Matrigel (Corning). Starting on day 6, when tumour volume reached around 100 mm³, Neo-2/15 and mouse IL-2 (Peprotech) were administered daily by intraperitoneal (i.p.) injection in 50 µl PBS (Gibco). Mice were euthanized when tumour volume reached 1,300 mm³. BALB/c mice were purchased from Charles River. Flow cytometry: all reagents were purchased from Gibco by Life Technologies (Thermo Fisher Scientific) unless stated otherwise. Excised tumours were minced and digested using a mix of collagenase I, collagenase IV (Worthington) and DNase I (Roche) in a shaker for 20 min, 250 r.p.m. at 37°C. After digestion, samples were passed through a 100-µm cell strainer, and resuspended in cold complete RPMI 1640 medium, supplemented with 10 mM HEPES buffer, 1 mM sodium pyruvate, 50 µM 2-mercaptoethanol, 100 U/ml penicillin and 100 µg/ml streptomycin and complemented with 1% non-essential amino acids (NEAA), 1% GlutaMAX supplement and 10% heat-inactivated FBS (HI FBS). The cell suspensions from the spleens and the inguinal lymph nodes were obtained through the smashing of the tissues against the filter of a 100-µm cell strainer. Cells were resuspended in PBS with 2% FBS and 1 mM EDTA and stained for extracellular markers for 45 min at 4°C. Cell suspensions were then fixed, permeabilized and stained for intracellular markers using the eBioscience Foxp3 Transcription Factor Staining Buffer Set from ThermoFisher Scientific. Samples were analysed in a BD LSRFortessa flow cytometer equipped with a BD FACSDiva software and data were analysed in FlowJo v.10 software and the statistical analysis was performed using Prism 5. Antibodies (BioLegend) used in colon carcinoma experiments were: CD45-BV510 (30-F11), CD3-BV711 (17A2), CD49b-FITC (DX5), CD4-BV605 (RM4-5), CD8-PECy7 (53-6.7), and Foxp3-APC (FJK-16 s; eBioscience). Fixable Viability Dye eFluor 780 (eBioscience) was used to exclude dead cells. Animals were maintained according to protocols approved by the Direção Geral de Veterinária and iMM Lisboa ethical committee.

Melanoma in vivo experiments. B16F10 cells were purchased from ATCC. On day 0, 5×10^5 cells were inoculated into the mice (C57BL/6J purchased from Jackson) by subcutaneous injection in 500 µl Hank's balanced salt solution (Gibco). Starting on the specified day, Neo-2/15 or mouse IL-2 (Peprotech) treatments were administered daily by intraperitoneal injection in 200 µl LPS-free PBS (Teknova). Treatment with TA99 (a gift from N. Momin and D. Wittrup, Massachusetts Institute of Technology) at 150 µg per mouse was added later on the day indicated in the text. Mice were euthanized when tumour volume reached 2,000 mm³. Flow cytometry: excised tumours were minced, enzymatically digested (Miltenyi Biotec), and passed through a 40-µm filter. Cells from spleens and tumour-draining lymph nodes were dispersed into PBS through a 40-µm cell strainer using the back of a 1-mL syringe plunger. All cell suspensions were washed once with PBS, and the cell pellet was resuspended in 2% inactivated fetal calf serum containing fluorophore-conjugated antibodies. Cells were incubated for 15 min at 4°C then fixed, permeabilized, and stained using a BioLegend FoxP3 staining kit. Samples were analysed on a BD Fortessa flow cytometer. Antibodies (BioLegend) used in melanoma experiments were: CD45-BV711 (clone 30-F11), CD8-BV650 (53-6.7), CD4-BV421 (GK1.5), TCRβ-BV510 (H57-597), CD25-AF488 (PC61), FoxP3-PE (MF-14). Animals were maintained according to

protocols approved by Dana-Farber Cancer Institute (DFCI) Institutional Animal Care and Use Committee.

Generation of anti-Neo-2/15 polyclonal antibody. Mice (C57BL/6J purchased from Jackson) were injected intraperitoneally with 500 µg of KO Neo-2/15 in 200 µl of a 1:1 emulsion of PBS and complete Freund's adjuvant. Mice were boosted on days 7 and 15 with 500 µg of KO Neo-2/15 in 200 µl of a 1:1 emulsion of PBS and incomplete Freund's adjuvant. On day 20, serum was collected and recognition of Neo-2/15 was confirmed by ELISA. For the ELISA, plates were coated with Neo-2/15, KO Neo-2/15, or mouse IL-2 mixed with ovalbumin for a total of 100 ng/well in carbonate buffer. Coated plates were incubated with mouse serum diluted 1:1,000 in PBS. Binding was detected using anti-mouse IgG conjugated to horseradish peroxidase (HRP) and developed with 3,3',5,5-tetramethylbenzidine (TMB). Results were quantified using absorption at 450 nm.

Enzyme-linked immunosorbent assay. High-binding 96-well plates (Corning) were coated overnight at 4°C with 100 ng/ml of Neo-2/15, mouse IL-2 (Peprotech), HsIL-2 (Peprotech) or ovalbumin (Sigma-Aldrich) in carbonate buffer. Antibody binding to target proteins was detected using HRP-conjugated sheep anti-mouse IgG (GE Healthcare) at 75 ng/ml. Plates were developed with tetramethylbenzidine and HCl. Absorbance was measured at 450 nm with an EnVision Multimode Plate Reader (PerkinElmer).

T cell proliferation assay. Cells were isolated from mice (C57BL/6J purchased from Jackson) spleens using the EasySep T Cell Isolation Kit (StemCell Technologies). Cells were plated in RPMI in 96-well culture plates at a density of 10,000 cells/well. Medium was supplemented with regular or heat-treated Neo-2/15, mouse IL-2, or super-2 (as indicated). After 5 days of incubation at 37°C, cell survival and proliferation were measured by CellTiter-Glo Luminescent Cell Viability Assay (Promega).

In vivo experiments. For T_{reg} expansion experiments (Fig. 4a), naive C57BL/6 mice were treated daily with Neo-2/15 or mouse IL-2 at the indicated concentrations ($n = 2$ –3 per group). After 14 days, spleens were harvested and analysed by flow cytometry using the indicated markers. For immunogenicity experiments (Fig. 4c), C57BL/6 mice were inoculated with 5×10^5 B16F10 cells by subcutaneous injection. Starting on day 1, mice were treated daily with Neo-2/15 (10 µg) or equimolar mouse IL-2 by intraperitoneal injection ($n = 10$ for each group). After 14 days, serum (antisera) was collected and IgG was detected by ELISA in plates coated with 10% fetal bovine serum (negative control), Neo-2/15, mouse IL-2, human IL-2, or ovalbumin as a negative control. Polyclonal mouse IgG against Neo-2/15 (anti-Neo-2/15 polyclonal antibody) was generated using complete Freund's adjuvant in conjunction with KO Neo-2/15, an inactive double point mutant of Neo-2/15: Y14D, F99D. For colorectal cancer experiments (Fig. 4d), BALB/C mice were inoculated with CT26 tumours. Starting on day 6, mice were treated daily by intraperitoneal injection of mouse IL-2 or Neo-2/15 (10 µg), or left untreated ($n = 5$ per group); For melanoma experiments (Fig. 4e), C57BL/6 mice were inoculated with B16 tumours. Starting on day 1, mice were treated daily by intraperitoneal injection of Neo-2/15 (10 µg) or equimolar mouse IL-2 ($n = 10$ per group). Twice-weekly treatment with TA99 was added on day 3. Mice were euthanized when weight loss exceeded 10% of initial weight or when tumour size reached 2,000 mm³; For CD8⁺: T_{reg} ratio in melanoma experiments (Fig. 4f), C57BL/6 mice were inoculated with B16 tumours and treated by daily intraperitoneal injection as indicated. Treatment with TA99 was started on day 5 and continued twice-weekly. Tumours were collected from mice when they reached 2,000 mm³, and were analysed by flow cytometry. The CD8⁺: T_{reg} cell ratio was calculated by dividing the percentage of CD45⁺TCR β ⁺ cells that were CD8⁺ by the percentage that were CD4⁺CD25⁺FoxP3⁺.

CAR-T cell in vivo experiments. In vitro T cell proliferation assay. Primary human T cells were obtained from healthy donors, who provided written informed consent for research protocols approved by the Institutional Review Board of the FHCRC. Peripheral blood mononuclear cells (PBMC) were isolated by centrifugation over Ficoll-Hypaque (Sigma). T cells were isolated using EasySep CD8 or CD4 negative isolation kits (Stemcell Technologies). To stimulate T cells, T cells were thawed and incubated with anti-CD3/CD28 Dynabeads (Gibco) at 1:1 ratio in medium supplemented with 50 IU/ml (3.1 ng/ml) IL-2. Beads were removed after four days of incubation. Stimulated or freshly thawed unstimulated T cells were plated at 30,000 or 50,000 cells/well, respectively, in 96-well format and cultured in indicated concentrations of IL-2 or Neo-2/15 in triplicate. Three days later, proliferation was measured using CellTiter-Glo 2.0. (Promega). In vivo RAJI experiment: the FHCRC Institutional Animal Care and Use Committee approved all mouse experiments. Six-to-eight-week-old NSG mice were obtained from the Jackson Laboratory. RAJI tumour cells (0.5×10^6) transduced with (ffLuc)-eGFP were injected into the tail vein of NSG mice. Seven days after tumour injection, lentiviral transduced anti-CD19 CAR T cells (0.4×10^6 CD4⁺, 0.4×10^6 CD8⁺) prepared as described⁷⁰ were infused intravenously into mice. Human IL-2 or Neo-2/15 at 20 µg/mouse was injected intraperitoneally from day 8 to 16 after tumour injection.

Disulfide-stapling Neo-2/15 to increase its stability and binding potency. Neo-2/15 is highly modular; this makes it possible to further tune its properties. As proof of concept, we designed stability-enhancing disulfide staples that preserve the function of the protein⁷¹. Two computational design strategies were tested. First, we designed internal disulfide bridges for all pairs of positions with favourable geometrical arrangements inside of Neo-2/15. The four best disulfide-stapled designs (that is, with the most favourable energy and minimal geometric distortion) were recombinantly expressed in *E. coli*. A design that bridges residues 38–75 (stabilizing helices H3→H2') was confirmed to be monomeric by size-exclusion chromatography followed by multi-angle light scattering (SEC-MALS). In the second approach, we remodelled the N- and C- termini of Neo-2/15 to allow the introduction of a single-disulfide staple encompassing the entire protein. We generated a total of 330 models that were then filtered based on fragment quality and disulfide-bond geometry. Finally, the designs were manually inspected and six were selected (representing a diversity of insertion lengths) and experimentally characterized as described above. One design, replacing the terminal residues P and S with the amino acid sequences CNSN and NFQC at the N and C termini, respectively (Extended Data Fig. 3) was confirmed to be monomeric by SEC-MALS. The designs from both disulfide-stapling strategies successfully increased the stability of Neo-2/15 ($T_m > 95^\circ\text{C}$) and its binding potency (Extended Data Fig. 3).

Pharmacodynamics and pharmacokinetics of Neo-2/15 in mice. We assessed the in vivo duration of pSTAT5 signalling response to Neo-2/15 in peripheral blood lymphocytes of naive mice (CD8 and B cells, Extended Data Fig. 6). As expected, Neo-2/15 has a substantial effect (similar to mouse IL-2) in CD8 cell signalling 1 h after administration, but as expected from the small size of Neo-2/15, the signalling effect decreases greatly after 3 h (Extended Data Fig. 6) and is undetectable after 8 h (data not shown). This suggests that future engineering of Neo-2/15 to extend half-life may be possible; there are a number of approaches such as Fc fusions, site-specific PEGylation (for example, through engineered cysteines, such as those demonstrated in Supplementary Fig. 14), fusions to targeting domains (for example, mAbs, sdAbs or VHVs^{12,72}, DARPins⁷², or de novo designed binding proteins^{35,73,74}) that can be used to extend its half-life and would likely translate into improved pharmacokinetics.

Molecular dynamics simulations of apo Neo-2/15 and holo Neo-2/15. Molecular dynamics simulations in explicit water solvent initiated from the computational model of apo Neo-2/15 recapitulated the crystallographic structure of (monomeric) apo Neo-2/15 (average r.m.s.d. to crystal structure = 1.9 Å; Extended Data Fig. 7a). For instance, molecular dynamics simulations initiated from the ternary complex of Neo-2/15 with the mouse IL-2R $\beta\gamma_c$ were more likely to sample the crystallographic structure observed for Neo-2/15 in the ternary complex with mouse IL-2R $\beta\gamma_c$, including the outward movement of helices H2'–H4 (Neo-2/15 average r.m.s.d. to crystal structure = 1.4 Å; Extended Data Fig. 7c). The conformation of Neo-2/15 seems to be stabilized in the ternary complexes (either with the mouse or human receptors; Extended Data Fig. 7c, d). Molecular dynamics simulations were performed using GROMACS 2018.1^{75,76} with the Amber99SB-ILDN force field⁷⁷. Each system consisted of the protein in a solvated dodecahedron box (minimum initial distance from the protein to the boundary = 1 nm) filled with explicit TIP3P waters⁷⁸ and neutralized with Cl⁻ or Na⁺ ions. The solvated systems were energy-minimized using the steepest descent minimization method, followed by equilibration for 200 ps under the NPT ensemble with position restraints (1,000 kJ mol⁻¹ nm⁻¹, applied on all the heavy atoms of the protein). Pressure coupling to 1 atm was performed with the Berendsen barostat⁷⁹, and the temperature was coupled to 310 K using the velocity-rescaling thermostat. The equilibrated systems were used as starting conformations for production runs. In the case of the monomers, we performed 5 independent production simulations of 100 ns each, and for the complexes bound to any of the IL-2 receptors, we performed 5 independent simulations of 90 ns each. The production simulations were conducted under the NPT ensemble, with the Parrinello–Rahman barostat⁸⁰ for pressure coupling to 1 atm. The cut-off for van der Waals and short-range electrostatic interactions was set to 1 nm. Long-range electrostatic interactions were treated with the particle-mesh Ewald (PME) summation method⁸¹, and the Verlet cut-off scheme was used⁸². The LINCS algorithm was used to constrain all chemical bonds and allow an integration time-step of 2 fs. The simulation trajectories were recorded every 20 ps and were analysed using GROMACS.

Statistical and power analyses. For statistical test a *P* value of less than 0.05 considered significant unless otherwise noted. For comparison of fitted curves in cellular phospho-STAT5 signalling assays, differences in EC₅₀ values were considered statistically significant if their 95% confidence intervals did not overlap. In vivo airway inflammation experiments; comparison of cell populations were performed using a two-tailed *t*-test. In vivo mouse colon cancer experiments; comparisons of the survival of tumour-bearing mice were performed using the log-rank Mantel–Cox test (95% confidence interval). Comparisons of weight loss in tumour-bearing mice were performed using a two-tailed *t*-test. In vivo mouse melanoma experiments:

comparisons of the survival of tumour-bearing mice were performed using the log-rank Mantel–Cox test (95% confidence interval). Comparisons of weight loss in tumour-bearing mice were performed using a two-tailed *t*-test. The minimum group size was determined using G*Power for an expected large effect size (Cohen's *d* = 1.75). For all the bar plots, the whiskers represent \pm s.d. and individual data points are shown (as dots) for experiments where the *n* < 5. Unless otherwise noted, results were analysed by one-way ANOVA, if significant (95% confidence interval), post hoc *t*-tests were performed comparing groups, and *P* values were adjusted for multiple comparisons are reported.

Software. The design of de novo protein mimics was performed using the custom Python code ‘protein mimic designer’ (<https://www.python.org>), IPython⁸³, and using the scientific high-performance modules: PyRosetta⁴², numpy and scipy^{84,85}, matplotlib⁸⁶, sklearn⁸⁷, cython⁸⁸ and pandas⁸⁹. Data analyses were performed with custom code in Python and IPython. Protein sequence design was performed with Rosetta^{40,41} and RosettaScripts⁴⁰. Protein visualization was performed using PyMOL⁵⁶. Simple protein–protein sequence alignments were performed using BLASTP, and structural based sequence comparisons were performed using MICAN⁹⁰. Sequence logos were generated with WebLogo⁹¹.

Reporting summary. Further information on research design is available in the Nature Research Reporting Summary linked to this paper.

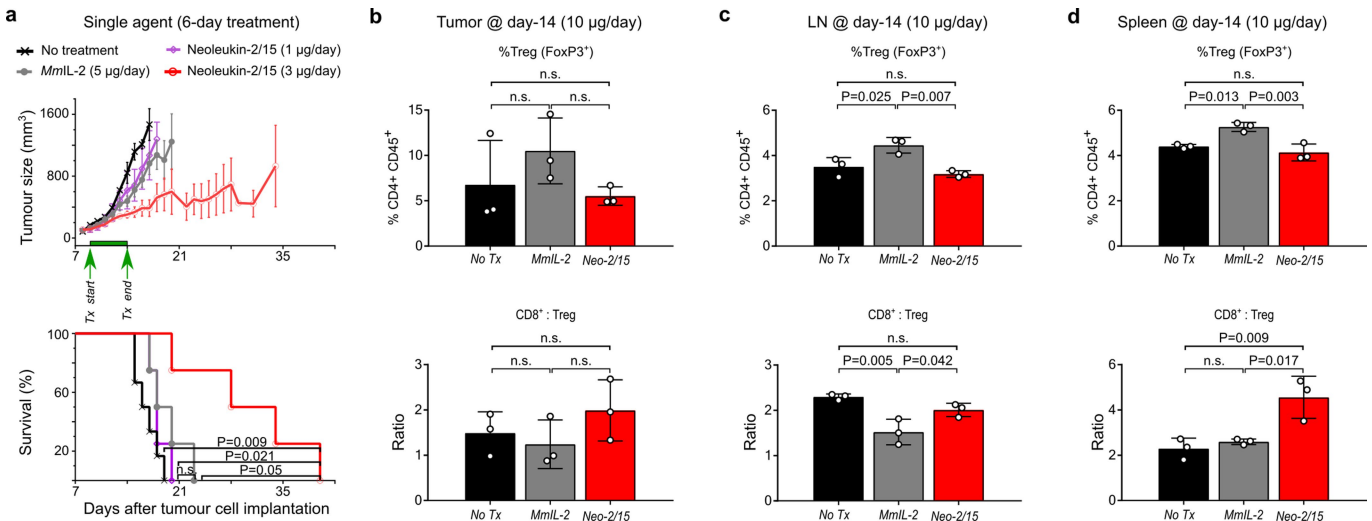
Code availability. The Python implementation of the de novo protein mimetic design algorithm (generation 2) and the clustered fragments database used for designing the de novo protein mimetics are available as part of the Rosetta distribution (<https://www.rosettacommons.org>) under the submodule ‘pyrosetta_scripts/apps/deNovoProteinDesign/deNovoProteinMimeticsGen2/’. Other code is available upon request.

Data availability

Structures for Neo-2/15 monomer and its ternary complex with mouse IL-2R $\beta\gamma_c$ have been deposited in the Protein Data Bank with accession numbers 6DG6 and 6DG5, respectively. Diffraction images have been deposited in the SBGrid Data Bank with accession numbers 587 and 588, respectively, and validation reports are included in the Supplementary Information. Other data and materials are available upon request from the corresponding authors.

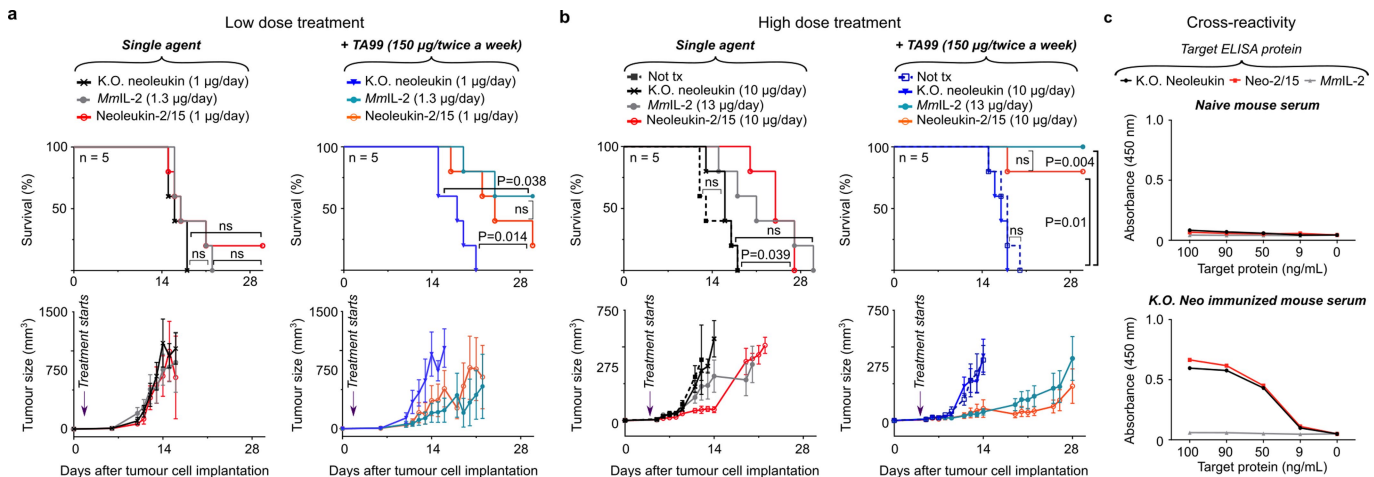
51. Fleishman, S. J. et al. Computational design of proteins targeting the conserved stem region of influenza hemagglutinin. *Science* **332**, 816–821 (2011).
52. Benattul, L., Perez, J. M., Belk, J. & Hsieh, C.-M. An improved yeast transformation method for the generation of very large human antibody libraries. *Protein Eng. Des. Sel.* **23**, 155–159 (2010).
53. Chang, H. C. et al. A general method for facilitating heterodimeric pairing between two proteins: application to expression of alpha and beta T-cell receptor extracellular segments. *Proc. Natl. Acad. Sci. USA* **91**, 11408–11412 (1994).
54. Kabsch, W. XDS. *Acta Crystallogr. D* **66**, 125–132 (2010).
55. Evans, P. Scaling and assessment of data quality. *Acta Crystallogr. D* **62**, 72–82 (2006).
56. Evans, P. R. & Murshudov, G. N. How good are my data and what is the resolution? *Acta Crystallogr. D* **69**, 1204–1214 (2013).
57. Winn, M. D. et al. Overview of the CCP4 suite and current developments. *Acta Crystallogr. D* **67**, 235–242 (2011).
58. McCoy, A. J. et al. Phaser crystallographic software. *J Appl. Crystallogr.* **40**, 658–674 (2007).
59. Terwilliger, T. C. et al. Iterative model building, structure refinement and density modification with the PHENIX AutoBuild wizard. *Acta Crystallogr. D* **64**, 61–69 (2008).
60. Emsley, P. et al. Features and development of Coot. *Acta Crystallogr. D* **66**, 486–501 (2010).
61. Adams, P. D. et al. PHENIX: a comprehensive Python-based system for macromolecular structure solution. *Acta Crystallogr. D* **66**, 213–221 (2010).
62. D'Arcy, A. et al. Microseed matrix screening for optimization in protein crystallization: what have we learned? *Acta Crystallogr. F* **70**, 1117–1126 (2014).
63. Bruhn, J. F. et al. Crystal structure of the Marburg virus VP35 oligomerization domain. *J. Virol.* **3**, e01085–16 (2017).
64. Smart, O. S. et al. Exploiting structure similarity in refinement: automated NCS and target-structure restraints in BUSTER. *Acta Crystallogr. D* **68**, 368–380 (2012).
65. The PyMOL Molecular Graphics System v2.1.0 (Schrodinger, LLC., 2010).
66. Morin, A. et al. Collaboration gets the most out of software. *eLife* **2**, e01456 (2013).
67. Yodoi, J. et al. TCGF (IL 2)-receptor inducing factor(s). I. Regulation of IL 2 receptor on a natural killer-like cell line (YT cells). *J. Immunol.* **134**, 1623–1630 (1985).
68. Kuziel, W. A., Ju, G., Grdina, T. A. & Greene, W. C. Unexpected effects of the IL-2 receptor alpha subunit on high affinity IL-2 receptor assembly and function detected with a mutant IL-2 analog. *J. Immunol.* **150**, 3357–3365 (1993).
69. Hondowicz, B. D. et al. Interleukin-2-dependent allergen-specific tissue-resident memory cells drive asthma. *Immunity* **44**, 155–166 (2016).

70. Liu, L. et al. Inclusion of Strep-Tag II in design of antigen receptors for T-cell immunotherapy. *Nat. Biotechnol.* **34**, 430–434 (2016).
71. Silva, D.-A., Stewart, L., Lam, K.-H., Jin, R. & Baker, D. Structures and disulfide cross-linking of de novo designed therapeutic mini-proteins. *FEBS J.* **285**, 1783–1785 (2018).
72. Stumpff, M. T., Kaspar Binz, H. & Amstutz, P. DARPinS: A new generation of protein therapeutics. *Drug Discov. Today* **13**, 695–701 (2008).
73. Marcos, E. & Silva, D.-A. Essentials of de novo protein design: methods and applications. *WIREs Comput. Mol. Sci.* **8**, e1374 (2018).
74. Berger, S. et al. Computationally designed high specificity inhibitors delineate the roles of BCL2 family proteins in cancer. *eLife* **5**, e20352 (2016).
75. Abraham, M. J. et al. GROMACS: High performance molecular simulations through multi-level parallelism from laptops to supercomputers. *SoftwareX* **1–2**, 19–25 (2015).
76. Markidis, S. & Laure, E. Solving software challenges for Exascale. In *International Conference on Exascale Applications and Software* (eds Markidis, S. & Laure, E.) (Springer, 2015).
77. Lindorff-Larsen, K. et al. Improved side-chain torsion potentials for the Amber ff99SB protein force field. *Proteins* **78**, 1950–1958 (2010).
78. Leszczynski, J. & Shukla, M. K. *Practical Aspects of Computational Chemistry: Methods, Concepts and Applications* (Springer, Dordrecht, 2009).
79. Berendsen, H. J. C., Postma, J. P. M., van Gunsteren, W. F., DiNola, A. & Haak, J. R. Molecular dynamics with coupling to an external bath. *J. Chem. Phys.* **81**, 3684–3690 (1984).
80. Parrinello, M. & Rahman, A. Polymorphic transitions in single crystals: A new molecular dynamics method. *J. Appl. Phys.* **52**, 7182–7190 (1981).
81. Essmann, U. et al. A smooth particle mesh Ewald method. *J. Chem. Phys.* **103**, 8577–8593 (1995).
82. Páll, S. & Hess, B. A flexible algorithm for calculating pair interactions on SIMD architectures. *Comput. Phys. Commun.* **184**, 2641–2650 (2013).
83. Perez, F. & Granger, B. E. IPython: a system for interactive scientific computing. *Comput. Sci. Eng.* **9**, 21–29 (2007).
84. Oliphant, T. E. Python for scientific computing. *Comput. Sci. Eng.* **9**, 10–20 (2007).
85. Oliphant, T. E. *Guide to NumPy* 2nd edn (CreateSpace, 2015).
86. Hunter, J. D. Matplotlib: a 2D graphics environment. *Comput. Sci. Eng.* **9**, 90–95 (2007).
87. Garreta, R. & Moncecchi, G. *Learning scikit-learn: Machine Learning in Python*. (Packt, Birmingham, 2013).
88. Behnel, S. et al. Cython: the best of both worlds. *Comput. Sci. Eng.* **13**, 31–39 (2011).
89. McKinney, W. *Python for Data Analysis: Data Wrangling with Pandas, NumPy, and IPython*. (O'Reilly, Sebastopol, 2017).
90. Minami, S., Sawada, K. & Chikenji, G. MICAN: a protein structure alignment algorithm that can handle multiple-chains, inverse alignments, C_α only models, alternative alignments, and non-sequential alignments. *BMC Bioinformatics* **14**, 24 (2013).
91. Crooks, G. E., Hon, G., Chandonia, J.-M. & Brenner, S. E. WebLogo: a sequence logo generator. *Genome Res.* **14**, 1188–1190 (2004).



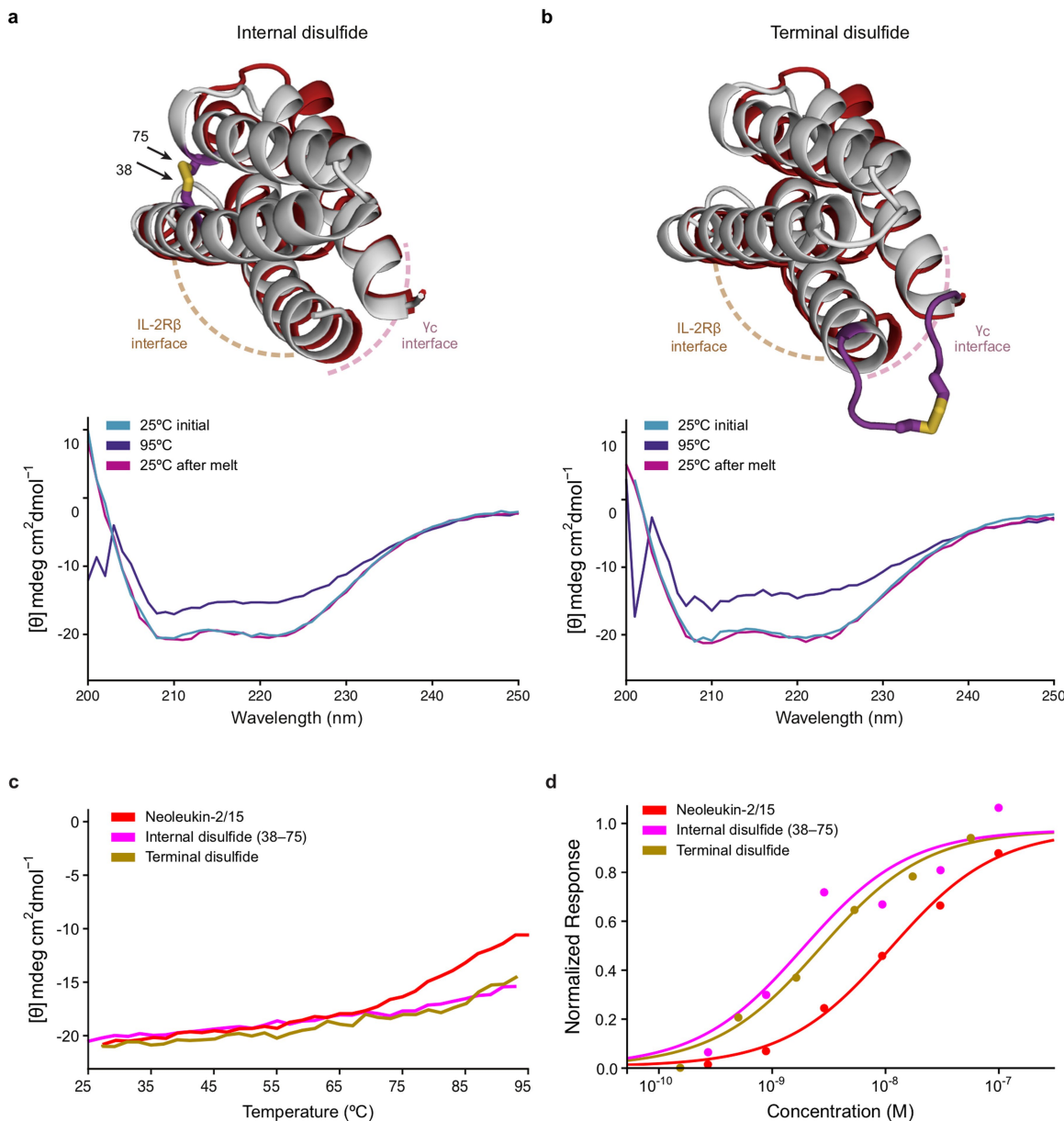
Extended Data Fig. 1 | Therapeutic effect of Neo-2/15 on colon cancer.
a, BALB/C mice were inoculated with CT26 tumours. Starting on day 9 and ending on day 14, mice were treated daily with intraperitoneal injection of mouse IL-2 or Neo-2/15 at the specified concentrations ($n = 4$ per group), or were left untreated ($n = 6$ per group). Top, tumour growth curves show data only for surviving mice and stop if the number of mice in a group fell below 50% of the initial number. Bottom, survival curves. Mice were euthanized when weight loss exceeded 10% of initial weight or when tumour size reached $1,300 \text{ mm}^3$. The experiments were performed twice with similar results. **b–d**, Bar plots comparing the T cell populations in BALB/C mice ($n = 3$ per group) that were inoculated with CT26

tumours and treated, starting from day 6, by daily intraperitoneal injection of 10 µg Neo-2/15, 10 µg mouse IL-2 or no treatment (no tx). On day 14 the percentage of T_{reg} cells (CD4⁺CD45⁺FoxP3⁺, top) and CD8:T_{reg} cell ratio (CD45⁺CD3⁺CD8⁺ cells:T_{reg} cells; bottom) were assessed in tumours (b), neighbouring inguinal lymph node (LN) (c), and spleen (d). Data are mean \pm s.e.m. Results were analysed by one-way ANOVA (95% confidence interval), except for survival curves that were assessed using the Mantel–Cox test (95% confidence interval). Experiments were performed twice with similar results.



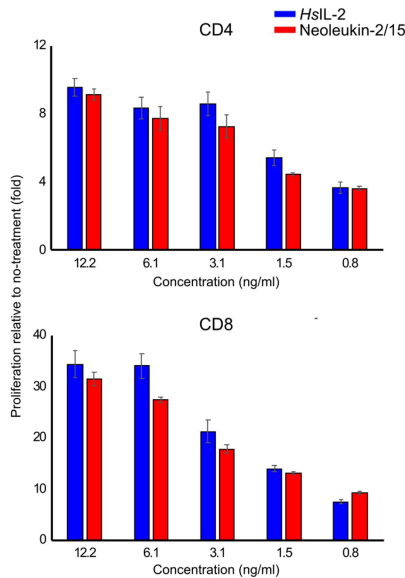
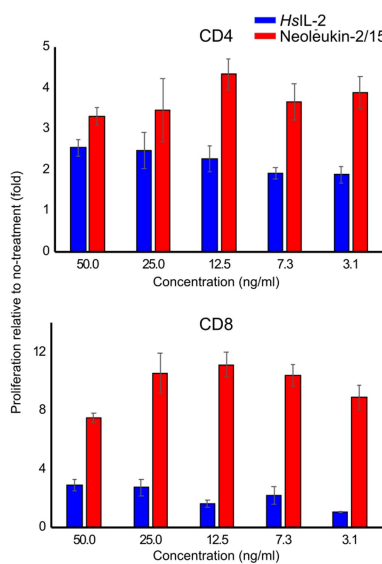
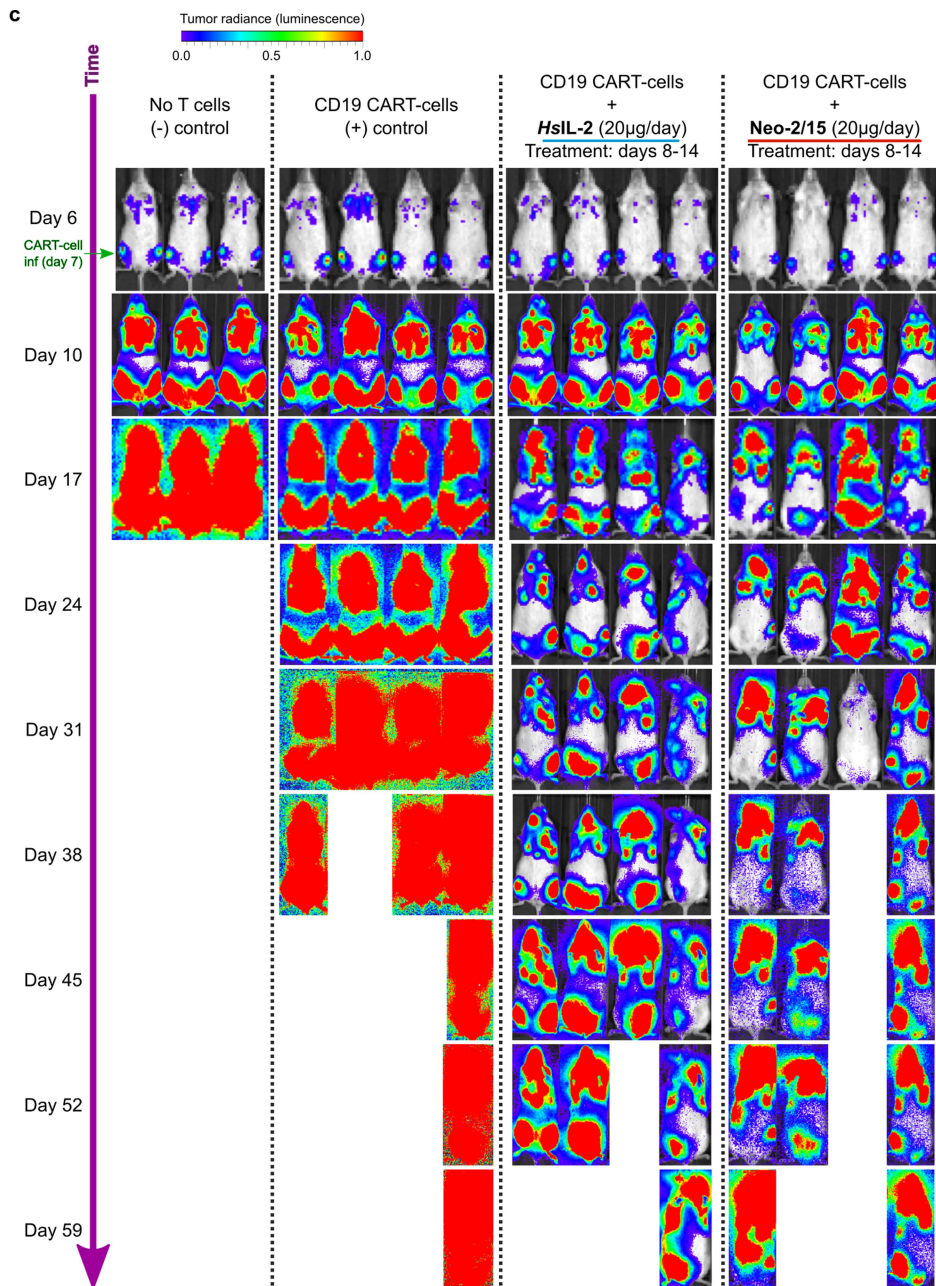
Extended Data Fig. 2 | Therapeutic effect of Neo-2/15 on melanoma. Survival curves (top) and tumour growth curves (bottom) for C57BL/6 mice that were inoculated with B16 tumours (as in Fig. 4a) and treated with low (1 µg per mouse per day) or high (10 µg per mouse per day) doses of Neo-2/15. **a**, Starting on day 1, mice ($n = 5$ per group) were treated daily with intraperitoneal injection of single agent Neo-2/15 at 1 µg per mouse or equimolar mouse IL-2 (left), or the same treatments in combination with a twice-weekly treatment with TA99 (started on day 5) (right). Mice were euthanized when tumour size reached 2,000 mm³. Tumour growth curves show data only for surviving mice and stop if the number of mice in a group fell below 50% of the initial number. The experiments were performed twice with similar results. **b**, Similar to **a**, but starting on day 4. Mice ($n = 5$ per group) were treated daily with intraperitoneal injection of single agent Neo-2/15 at 10 µg per mouse or equimolar mouse IL-2 (left), or the same treatments in combination with a twice-weekly treatment with TA99 (started on day 4) (right). Mice were euthanized when tumour size reached 1,000 mm³. The therapeutic effect of Neo-2/15 is dose-

dependent (higher doses have a stronger effect) and is potentiated in the presence of the antibody TA99. Tumour growth curves show data only for surviving mice and stop if the number of mice in a group fell below 50% of the initial number. The experiments were performed twice with similar results. **c**, C57BL/6 mice were immunized with 500 µg KO Neo-2/15 in complete Freund's adjuvant and boosted on days 7 and 15 with 500 µg KO Neo-2/15 in incomplete Freund's adjuvant. Reactivity against KO Neo-2/15 and native Neo-2/15, as well as cross-reactivity with mouse IL-2 were determined by incubation of serum (diluted 1:1,000 in PBS) with plate-bound KO Neo-2/15, Neo-2/15 or mouse IL-2 as indicated. Serum binding was detected using an anti-mouse secondary antibody conjugated to HRP followed by incubation with TMB. Data are reported as optical density at 450 nm. Top, naive mouse serum; bottom, immunized mouse serum. The experiments were performed once. In all the growth curves, data are mean \pm s.e.m. Results were analysed by one-way ANOVA (95% confidence interval), except for survival curves that were assessed using the Mantel–Cox test (95% confidence interval).



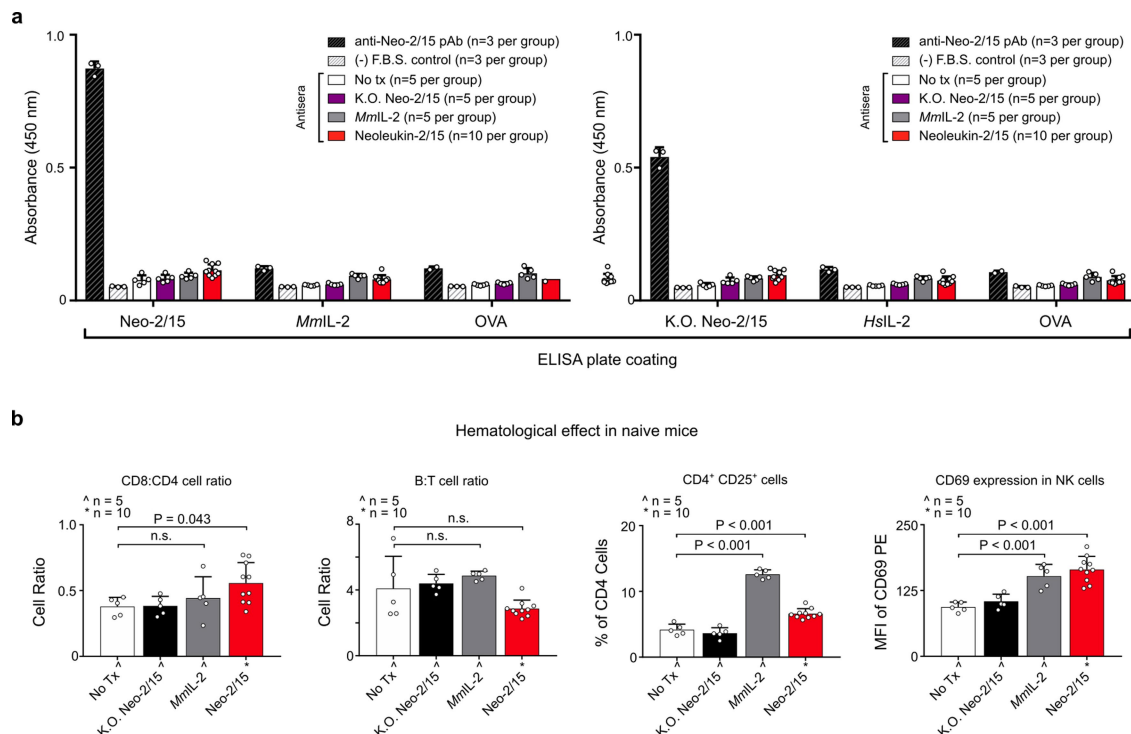
Extended Data Fig. 3 | Single disulfide-stapled variants of Neo-2/15 with higher thermal stability. **a, b,** Structural models of disulfide-stabilized variants of Neo-2/15 (grey) are shown superposed on the ternary crystal structure of Neo-2/15 (red) with mutated residues highlighted in magenta and the disulfide bond shown in gold. Two strategies were used to generate the disulfide stapled variants. **a,** Top, internal placement of the disulfide linking residues 38 and 75. Bottom, experimental CD spectra of the design at 25 °C, 95 °C and then cooled back to 25 °C, showing complete recovery of ellipticity spectrum (full reversibility) upon cooling. **b,** Top, for the terminal disulfide variant, three residues were added to each terminus in order to allow the disulfide to be formed without distorting the Neo-2/15 structure. Bottom, experimental CD spectra of the design at 25 °C, 95 °C and then cooled back to 25 °C, showing complete recovery of ellipticity spectrum (full reversibility) upon cooling. **c,** Thermal melting

of each disulfide variant in **a** and **b** between 25 °C and 95 °C (heating rate $\approx 2\text{ }^{\circ}\text{C min}^{-1}$) was monitored using circular dichroism at 222 nm. Each of the disulfide-stapled variants shows improved stability relative to native Neo-2/15. **d,** Binding strength of each disulfide variant was measured by biolayer interferometry, showing that the introduction of disulfide bonds does not disrupt binding. Furthermore, both disulfide variants exhibit improved binding of IL-2R $\beta\gamma_c$ ($K_d \approx 1.3 \pm 0.49\text{ nM}$ and $1.8 \pm 0.26\text{ nM}$ for the internal and external disulfide staples, respectively), compared to Neo-2/15 ($K_d \approx 6.9 \pm 0.61\text{ nM}$) under the same experimental conditions. These results are consistent with the expected effect of disulfide-induced stabilization on a de novo protein binding site⁷¹. Thermal denaturation experiments were performed 3 times with similar results; binding experiments were performed once.

a (in vitro) proliferation of stimulated T-cells**b (in vitro) proliferation of unstimulated T-cells****c**

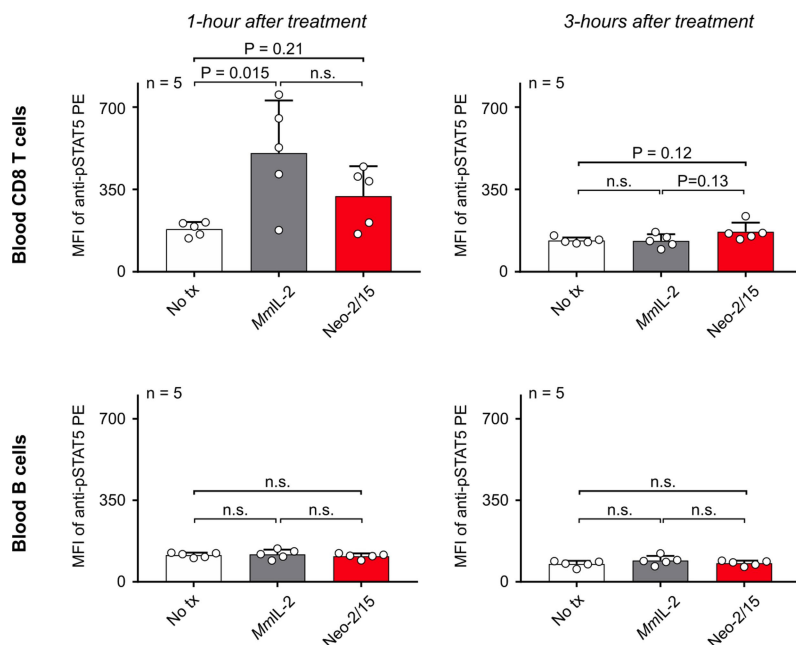
Extended Data Fig. 4 | The stimulatory effect of Neo-2/15 on human CAR-T cells. **a, b**, Human primary CD4 (top) or CD8 (bottom) T cells stimulated with CD3/CD28 antibodies (**a**) or unstimulated (**b**) were cultured in indicated concentrations of human IL-2 or Neo-2/15. T cell proliferation was measured as fold change over T cells cultured without

IL-2 supplement. Experiments were performed 3 times with similar results. Data are mean \pm s.d. **c**, NSG mice inoculated with 0.5×10^6 RAJI tumour cells were treated with 0.8×10^6 anti-CD19 CAR-T cells 7 days post-tumour inoculation. Tumour growth was analysed by bioluminescence imaging. The experiment was performed once.



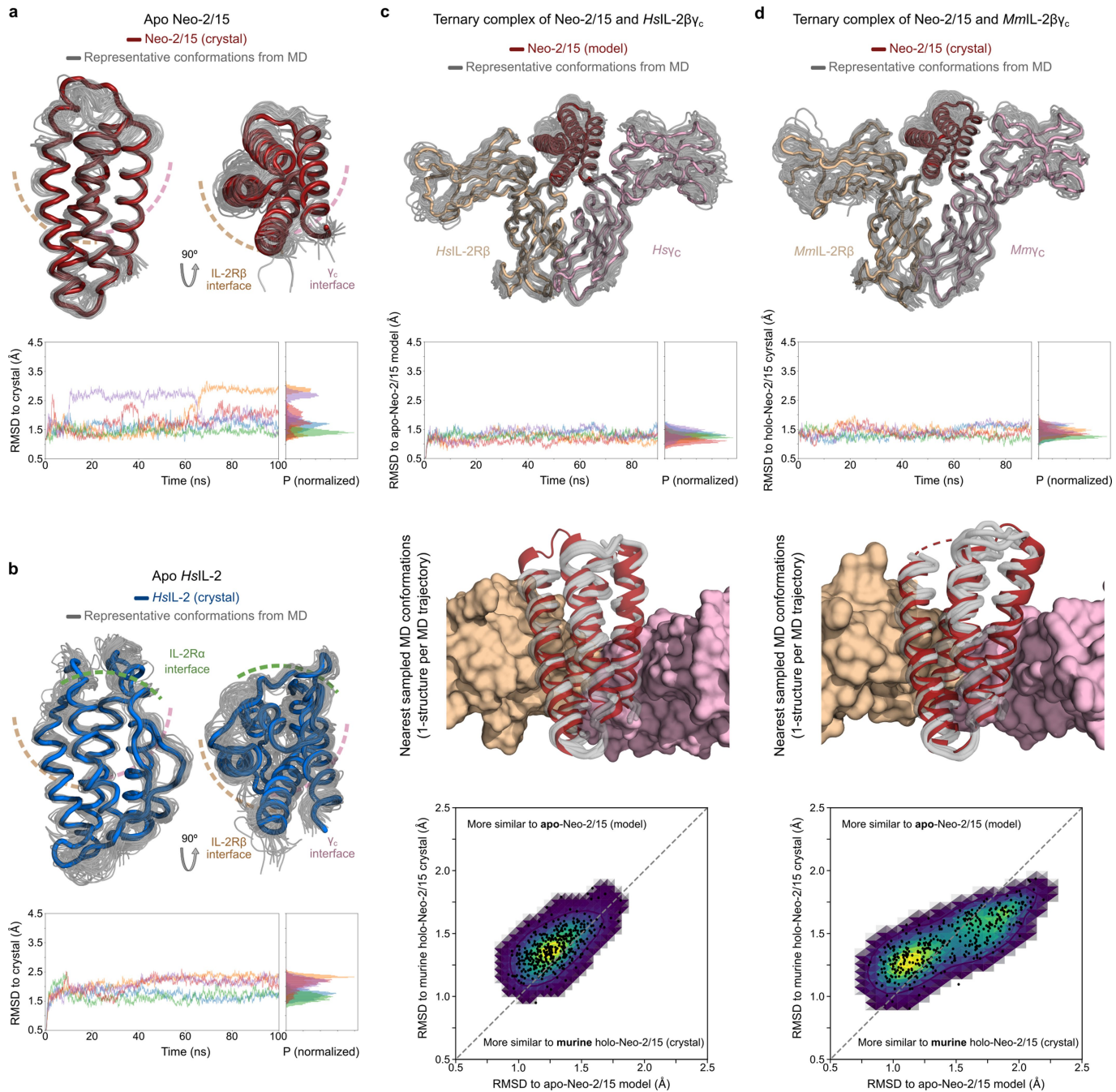
Extended Data Fig. 5 | Immunogenicity of Neo-2/15 in healthy naive mice. **a**, Naive C57BL/6 mice were treated daily with Neo-2/15 ($n = 10$), KO Neo-2/15 ($n = 5$), mouse IL-2 ($n = 5$) or left untreated ($n = 5$). Blood was collected after 28 days and the serum was diluted 1:100 and analysed for IgG against Neo-2/15, mouse IL-2, human IL-2, KO Neo-2/15 and ovalbumin using ELISA. FBS (10%) was used as a negative control. Polyclonal antibody against Neo-2/15 was used as a positive control. All statistical comparisons between sera from treated mice and negative control serum were not significant (two-way ANOVA with a 95% confidence interval). All statistical comparisons between Neo-2/15 and

mouse IL-2 treated mice serum were not significant (two-way ANOVA with a 95% confidence interval). The experiments were performed once. **b**, After 14 days, immune cell populations in the blood of treated mice were quantified by flow cytometry. B cell:T cell ratio (top right) was calculated by dividing the percentage of $B220^+$ cells by the percentage of $CD3^+$ cells. $CD8^+$ cell: $CD4^+$ cell ratio (top left) was calculated by dividing the percentage of $CD3^+CD8^+$ cells by the percentage of $CD3^+CD4^+$ cells. NK cells (bottom left) were identified by their expression of NK1.1. Results were analysed by one-way ANOVA (95% confidence interval). The experiments were performed once. In all cases, data are mean \pm s.d.



Extended Data Fig. 6 | Kinetics of STAT5 phosphorylation with Neo-2/15 treatment. Naive C57BL/6 mice were treated once with 13 µg mouse IL-2 ($n = 5$) or 10 µg Neo-2/15 ($n = 5$), or were left untreated ($n = 5$). Phosphorylation of STAT5 was measured in peripheral blood at the indicated time points by flow cytometry using an anti-pSTAT5 antibody.

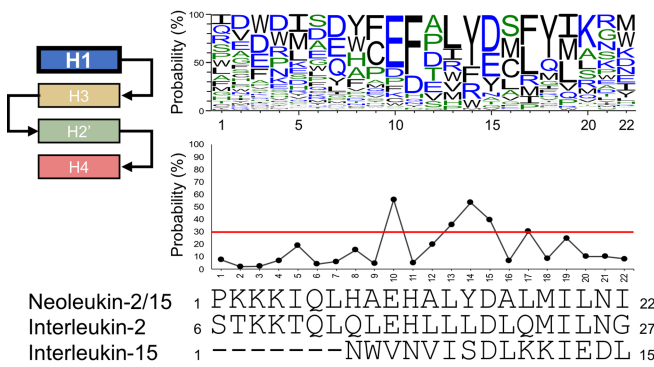
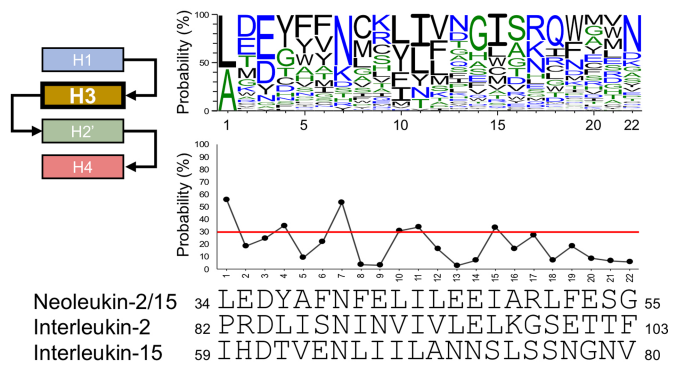
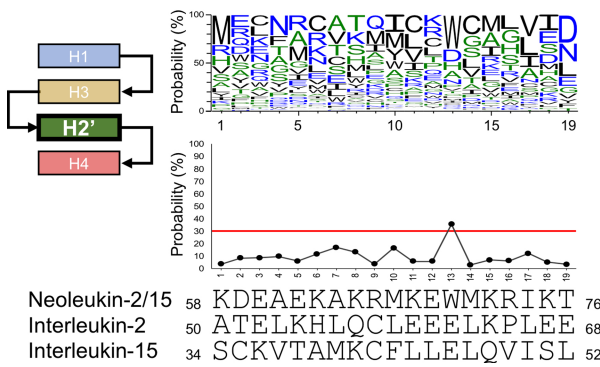
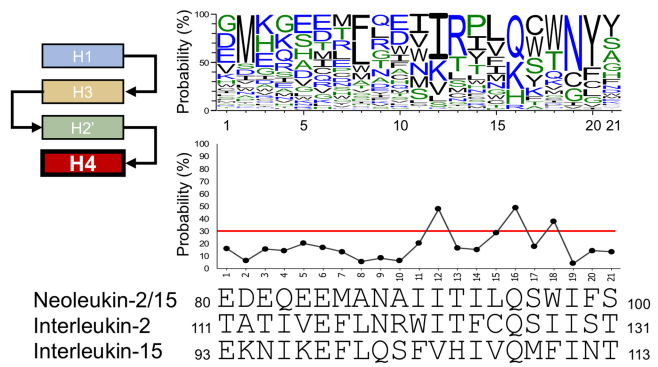
Mean fluorescence intensity (MFI) is shown at each time point for $\text{TCR}^{\beta^+}\text{CD8}^+$ cells (top) and $\text{TCR}^{\beta^-}\text{B220}^+$ cells (bottom). Data are mean \pm s.d. Results were analysed by one-way ANOVA (75% confidence interval). The experiments were performed once.



Extended Data Fig. 7 | See next page for caption.

Extended Data Fig. 7 | Conformational flexibility of Neo-2/15 in molecular dynamics simulations. **a**, Molecular dynamics simulations started from the computational model of Neo-2/15 (top) converged into structures similar to the crystal conformation. Apo Neo-2/15 is shown in red thick tubes (chain A from PDB ID: 6GD6) and 45 (randomly selected) molecular dynamics conformations from 5 independent simulations are shown in thin grey tubes. Bottom, the plot shows the r.m.s.d. along 5 independent simulations (average r.m.s.d. = 1.93 Å). **b**, Similar to **a**, but for (control) molecular dynamics simulations started from the crystallographic structure of human IL-2. Top, crystal conformation of human IL-2 (chain A from PDB ID: 2B5I) is shown in blue thick tubes and 45 (randomly selected) conformations from 5 independent molecular dynamics simulations are shown in thin grey tubes (average r.m.s.d. = 2.02 Å). **c**, Top, similar to **a** and **b**, but showing molecular dynamics structures for simulations started from the computational model of Neo-2/15 bound to human IL-2R $\beta\gamma_c$. The plot shows the r.m.s.d. along 5 independent molecular dynamics simulations (average r.m.s.d. to apo Neo-2/15 (model) = 1.28 Å). The lower structure shows the nearest conformation (to the apo Neo-2/15 computational model) that was sampled on each of the 5 independent simulations (structures from the first 50 ns of molecular dynamics simulations were not considered). Bottom, a 2D scatter plot (and the underlying density plot, in which yellow, blue, green and purple represent decreasing densities) comparing the r.m.s.d. (after discarding the first 50 ns of each simulation) for apo Neo-2/15 (computational model) versus the r.m.s.d. for the holo crystal

structure of Neo-2/15 (in complex with the mouse receptor). The conformations sampled by Neo-2/15 when in complex with human IL-2R $\beta\gamma_c$ are more similar to the apo Neo-2/15 structure (computational model) than to the Neo-2/15 conformation observed in complex with mouse IL-2R $\beta\gamma_c$. **d**, As in **c**, but for molecular dynamics simulations started from the computational model of apo Neo-2/15 in complex with the crystallographic structure of mouse IL-2R $\beta\gamma_c$. The model of apo Neo-2/15 was generated by aligning (using TMalign) the ternary computational model of Neo-2/15 with human IL-2R $\beta\gamma_c$ (from **c**) into our crystallographic structure of mouse IL-2R $\beta\gamma_c$ (PDB ID: 6GD5) (average r.m.s.d. to holo Neo-2/15 (mouse) = 1.43 Å). Bottom, 2D scatter plot (and the underlying density plot, in which yellow, blue, green and purple represent decreasing densities) comparing the r.m.s.d. (after discarding the first 50 ns of molecular dynamics simulation) for apo Neo-2/15 (computational model) versus the r.m.s.d. for the holo crystal structure of Neo-2/15 (in complex with the mouse receptor). Unlike in **c**, the conformations sampled by Neo-2/15 when in complex with mouse IL-2R $\beta\gamma_c$ are more similar to the Neo-2/15 conformation observed in the crystallographic structure of the ternary complex of Neo-2/15 with mouse IL-2R $\beta\gamma_c$ (Fig. 3). For clarity, all the r.m.s.d. plots were filtered (running average filter, 5 frames = 100 ps), and points in the 2D scatter plots were subsampled every 25 conformations (that is, every 500 ps); however, the density plot corresponds to all the analysed conformations (that is, the last 40 ns of 5 molecular dynamics simulations that were analysed, and conformations were recorded each 20 ps).

Helix 1 consensus**Helix 3 consensus****Helix 2' consensus****Helix 4 consensus**

Extended Data Fig. 8 | Overall sequence conservation in binding residues for each of the four common helices, combining information from the three different de novo-designed IL-2 mimics. Sequence logos were generated using combined data from binding experiments (using the heterodimeric mouse IL-2R $\beta\gamma$, see Methods) from 3 independent SSM mutagenesis libraries for G2_neo2_40_1F_seq27, G2_neo2_40_1F_seq29 and G2_neo2_40_1F_seq36 (Supplementary Figs. 8–10). All of these proteins are functional high-affinity mimetics of mouse and human IL-2 (see Supplementary Figs. 6–11), some having topologies that differ from that of Neo-2/15, but all containing the four Helices H1, H3, H2' and H4. The logos show the combined information for each helix independently.

Below each logo, a line graph shows the probability score (higher means more conserved) for each amino acid in the Neo-2/15 sequence. The red line highlights positions where the Neo-2/15 amino acid has a probability score $\geq 30\%$ (that is, these amino acids contribute more generally to receptor binding as they are globally enriched in the binding populations across all of the de novo IL-2 mimics tested). The topology of each helix in Neo-2/15 is shown left of each logo. The sequences of the Neo-2/15 helices and those of the corresponding helices (structurally aligned) in human IL-2 and IL-15 are shown below the graphs, highlighting the distinctiveness of the Neo-2/15 helices and binding interfaces.

Extended Data Table 1 | Characterization of several de novo designed mimics of IL-2/IL-15

Binding affinity (Kd) to <i>Hs</i> IL-2R β Yc, and cell signaling in human NK (YT, CD25-) cells								
Name	Kd <i>Hs</i> IL-2R β Yc (nM)	Kd <i>Hs</i> IL-2R β (nM)	EC50 (CD25+) pSTAT5p (nM) / (exp i.d.)	Seq identity to <i>Hs</i> IL-2 (% / (num a.a. align))	Seq identity to <i>Mm</i> IL-2 (% / (num a.a. align))	Exp. optimized	Parent molecule	a.a. length
<i>Hs</i> IL-2	193.6	326.9	0.41 / (a)	100.0 / (120)	54.5 / (112)	-	-	133
<i>Mm</i> IL-2	8034.0	4950.0	39.05 / (a)	54.5 / (112)	100 / (122)	-	-	130
Super-2 / Superkine (PDB: 3QAZ)	300.9	2.0	0.07 / (a)	94.9 / (117)	50.9 / (114)	Y	<i>Hs</i> IL-2	133
G1_neo2_40	260.0	1457.0	0.14 / (b)	47.7 / (86)	30.4 / (79)	N	-	87
G1_neo2_41	187.0	720.6	0.07 / (b)	47.7 / (86)	30.4 / (79)	N	-	87
G1_neo2_43	533.4	2861.0	0.21 / (b)	50.0 / (86)	32.9 / (79)	N	-	87
G1_neo2_40_1F	2.3	2.6	0.09 / (c)	44.2 / (86)	26.6 / (79)	Y	G1_neo2_40	87
G2_neo2_40_1F_dsn36	113.9	27.6	0.12 / (a)	33.7 / (89)	17.6 / (85)	N	<i>De novo</i> mimetic design inspired on template: G1_neo2_40_1F	
Neoleukin-2/15 (G2_neo2_40_1F_dsn36)	18.8	11.2	0.05 / (a)	29.2 / (89)	15.7 / (83)	Y	G2_neo2_40_1F_dsn36	100

Binding affinity (Kd) to <i>Mm</i> IL-2R β Yc, and cell signaling (EC50) in murine T (CTLL-2, CD25+) cells									
Name	Kd <i>Mm</i> IL-2R β Yc (nM)	Kd <i>Mm</i> IL-2R β (nM)	EC50 (CD25+) pSTAT5 (nM) / (exp i.d.)	Seq identity to <i>Hs</i> IL-2 (% / (num a.a. align))	Seq identity to <i>Mm</i> IL-2 (% / (num a.a. align))	Exp. optimized	Parent molecule	a.a. length	
<i>Hs</i> IL-2	492.2	8106.0	0.002 / (d)	*see top table					
<i>Mm</i> IL-2	126.2	1496.0	0.003 / (e)	*see top table					
Super-2 / Superkine (PDB: 3QAZ)	312.2	214.0	N/A	*see top table					
G1_neo2_40_1F	7.9	485.5	0.2 / (e)	*see top table					
G1_neo2_40_1F_H1	2654.0	6799.0	37.38 / (d)	39.5 / (86)	25.0 / (80)	Y	G1_neo2_40_1F	87	
G1_neo2_40_1F_H2	963.7	68300.0	9.38 / (d)	40.7 / (86)	26.2 / (80)	Y	G1_neo2_40_1F	87	
G1_neo2_40_1F_H3	3828.0	N/S	35.2 / (d)	39.5 / (86)	25.0 / (80)	Y	G1_neo2_40_1F	87	
G1_neo2_40_1F_H4	391.8	10070.0	0.93 / (d)	41.9 / (86)	26.2 / (80)	Y	G1_neo2_40_1F	87	
G1_neo2_40_1F_H5	5123.0	45300.0	84.69 / (d)	39.5 / (86)	23.8 / (80)	Y	G1_neo2_40_1F	87	
G1_neo2_40_1F_M1	4.3	213.9	0.007 / (d)	36.0 / (86)	25.0 / (80)	Y	G1_neo2_40_1F	87	
G1_neo2_40_1F_M2	886.3	2599.0	3.11 / (d)	37.2 / (86)	25.0 / (80)	Y	G1_neo2_40_1F	87	
G1_neo2_40_1F_M3	64.8	402.3	0.08 / (d)	34.9 / (86)	25.3 / (79)	Y	G1_neo2_40_1F	87	
G2_neo2_40_1F_seq04	80.0	N/A	1.95 / (f)	38.4 / (86)	23.8 / (80)	N	Sequence redesign of G1_neo2_40_1F		
G2_neo2_40_1F_seq12	39.1	N/A	1.74 / (f)	38.4 / (86)	25.3 / (79)	N	Sequence redesign of G1_neo2_40_1F		
G2_neo2_40_1F_seq16	71.5	N/A	2.20 / (f)	34.9 / (86)	22.5 / (80)	N	Sequence redesign of G1_neo2_40_1F		
G2_neo2_40_1F_seq26	27.8	N/A	1.06 / (f)	39.5 / (86)	25.3 / (79)	N	Sequence redesign of G1_neo2_40_1F		
G2_neo2_40_1F_seq27	13.6	N/A	0.24 / (f)	36.0 / (86)	25.0 / (80)	N	Sequence redesign of G1_neo2_40_1F		
G2_neo2_40_1F_dsn29	38.2	N/A	0.48 / (f)	36.6 / (82)	8.9 / (90)	N	De novo mimetic design using template: G1_neo2_40_1F		
G2_neo2_40_1F_dsn30	925.0	N/A	7.61 / (f)	33.0 / (97)	23.4 / (94)	N	De novo mimetic design using template: G1_neo2_40_1F		
G2_neo2_40_1F_dsn36	568.5	2432.0	1.36 / (e)	*see top table					
G2_neo2_40_1F_dsn40	69.2	N/A	0.50 / (f)	33.7 / (89)	17.9 / (84)	N	De novo mimetic design inspired on template: G1_neo2_40_1F		
Neoleukin-2/15 (G2_neo2_40_1F_dsn36)	38.4	16.1	0.07 / (e)	*see top table					

The table shows experimental and structural properties for several de novo mimics of IL-2/IL-15 mimics. Human IL-2, mouse IL-2, and super-2 are shown as references. The sequence similarity was calculated by structural alignment against human IL-2 (PDB ID: 2B5I) or mouse IL-2 (PDB ID: 4YQX). The EC₅₀ field refers to pSTAT5 cell signalling measured across 6 independent experiments (denoted by a-f in parentheses). N/S, not significant; N/A, not available. The binding and signalling experiments were performed 3 times with similar results.

Extended Data Table 2 | Crystallographic data table for monomeric Neo-2/15 and the quaternary complex of Neo-2/15 with mouse IL-2R $\beta\gamma_c$

	Neoleukin-2/15 (6DG6)	Neoleukin-2/15 ternary complex with <i>MmIL-2R$\beta\gamma_c$</i> (6DG5)
Data collection		
Space group	P 21 21 21	P 21 2 21
Cell dimensions		
<i>a</i> , <i>b</i> , <i>c</i> (Å)	73.73, 86.8, 92.31	65.125, 67.914, 172.084
α , β , γ (°)	90, 90, 90	90, 90, 90
Resolution (Å)	39.28 - 1.999 (2.07 - 1.999) ^d	47.005 - 2.516 (2.828 - 2.516)
Ellipsoidal ^a resolution limit (Å) (direction) ^b	-	3.422 (a) ^d 2.407 (b) ^d 3.475 (c) ^d
R_{sym}	0.1027 (1.709)	0.3590 (2.516)
$I/\sigma I$	12.19 (1.25)	6.8 (1.3)
Completeness (%)	92.58 (77.83)	52.3 (9.0)
Completeness (ellipsoidal) ^c (%)		93.2 (77.2)
Redundancy	8.7 (8.1)	9.5 (11.2)
Refinement		
Resolution (Å)	39.28 - 1.999 (2.07 - 1.999)	47.005 - 2.516
No. reflections	37747 (3125)	13923 (136)
$R_{\text{work}} / R_{\text{free}}$	0.2037/0.2260	0.2211/0.2658
No. atoms	4791	4100
Protein	4735	3949
Ligand/ion	0	138
Water	56	13
<i>B</i> -factors	52.56	47.05
Protein	52.54	46.39
Ligand/ion	-	67.79
Water	54.21	27.31
R.m.s. deviations		
Bond lengths (Å)	0.005	0.004
Bond angles (°)	0.88	0.94

^aStatistics are for data that were truncated by STARANISO to remove poorly measured reflections affected by anisotropy.^bThe resolution limits for three directions in reciprocal space are indicated here. To calculate this, STARANISO computed an ellipsoid post-fitted by least squares to the cut-off surface, removing points where the fit was poor. Note that the cut-off surface is unlikely to be perfectly ellipsoidal, so this is only an estimate.^cThe anisotropic completeness was obtained by least-squares fitting an ellipsoid to the reciprocal lattice points at the cut-off surface defined by a local mean $I/\sigma I$ threshold of 1.0, rejecting outliers in the fit owing to spurious deviations (including any cusp), and calculating the fraction of observed data lying inside the ellipsoid so defined. Note that the cut-off surface is unlikely to be perfectly ellipsoidal, so this is only an estimate.^dValues in parentheses are for the highest-resolution shell.

Reporting Summary

Nature Research wishes to improve the reproducibility of the work that we publish. This form provides structure for consistency and transparency in reporting. For further information on Nature Research policies, see [Authors & Referees](#) and the [Editorial Policy Checklist](#).

Statistical parameters

When statistical analyses are reported, confirm that the following items are present in the relevant location (e.g. figure legend, table legend, main text, or Methods section).

n/a Confirmed

- The exact sample size (n) for each experimental group/condition, given as a discrete number and unit of measurement
- An indication of whether measurements were taken from distinct samples or whether the same sample was measured repeatedly
- The statistical test(s) used AND whether they are one- or two-sided
Only common tests should be described solely by name; describe more complex techniques in the Methods section.
- A description of all covariates tested
- A description of any assumptions or corrections, such as tests of normality and adjustment for multiple comparisons
- A full description of the statistics including central tendency (e.g. means) or other basic estimates (e.g. regression coefficient) AND variation (e.g. standard deviation) or associated estimates of uncertainty (e.g. confidence intervals)
- For null hypothesis testing, the test statistic (e.g. F , t , r) with confidence intervals, effect sizes, degrees of freedom and P value noted
Give P values as exact values whenever suitable.
- For Bayesian analysis, information on the choice of priors and Markov chain Monte Carlo settings
- For hierarchical and complex designs, identification of the appropriate level for tests and full reporting of outcomes
- Estimates of effect sizes (e.g. Cohen's d , Pearson's r), indicating how they were calculated
- Clearly defined error bars
State explicitly what error bars represent (e.g. SD, SE, CI)

Our web collection on [statistics for biologists](#) may be useful.

Software and code

Policy information about [availability of computer code](#)

Data collection

The design of protein mimics was performed using custom code programmed in python and ipython, in combination with the scientific/high-performance modules: pyrosetta, numpy and scipy, matplotlib, sklearn, cython and pandas. Protein sequence design was performed using Rosetta and RosettaScripts. The computer code and examples are provided along with SI.

Data analysis

Data analysis was performed using custom code programmed in python and ipython and Rosetta, in combination with the scientific/high-performance modules: pyrosetta, numpy and scipy, matplotlib, sklearn, cython and pandas. Protein visualization was performed using PyMOL (PyMOL | pymol.org).

For manuscripts utilizing custom algorithms or software that are central to the research but not yet described in published literature, software must be made available to editors/reviewers upon request. We strongly encourage code deposition in a community repository (e.g. GitHub). See the Nature Research [guidelines for submitting code & software](#) for further information.

Data

Policy information about [availability of data](#)

All manuscripts must include a [data availability statement](#). This statement should provide the following information, where applicable:

- Accession codes, unique identifiers, or web links for publicly available datasets
- A list of figures that have associated raw data
- A description of any restrictions on data availability

PDBs for Neoleukin-2/15 monomer and for its ternary complex with mIL-2R β gc have been deposited in the RCSB protein data bank (PDB IDs: 6DG6 and 6DG5, respectively), diffraction images have been deposited in the SBGrid Data Bank (IDs: 587 and 588, respectively) and validation reports for each of the PDBs are part of the supplementary information. The databases of clustered fragments and the algorithms used for designing de novo protein mimetics (programmed as python/pyrosetta scripts) as described in this manuscript are available in the online repository Zenodo (ID: “to be provided with the final manuscript”). Other data and materials related to this manuscript are available upon request to the corresponding authors.

Field-specific reporting

Please select the best fit for your research. If you are not sure, read the appropriate sections before making your selection.

Life sciences Behavioural & social sciences Ecological, evolutionary & environmental sciences

For a reference copy of the document with all sections, see nature.com/authors/policies/ReportingSummary-flat.pdf

Life sciences study design

All studies must disclose on these points even when the disclosure is negative.

Sample size

Yeast display: Sample size was based on historical data which revealed statistical significance in previous experiments.
 In vitro Stat5 experiments: Sample size was based on historical data which revealed statistical significance in previous experiments.
 Ex vivo Stat5 experiments: Sample size was based on historical data which revealed statistical significance in previous experiments.
 In vivo Airway inflammation experiments: Sample size was based on historical data which revealed statistical significance in previous experiments.
 Colorectal carcinoma in vivo experiments: Sample size was based on historical data for similar colorectal cancer experiments, no statistical methods were used to pre-determine sample size.
 Melanoma in vivo experiments: The minimum group size was determined using G*Power for an expected large effect size (Cohen's d = 1.75).
 Car-T cells in vivo experiments: Sample size was based on historical data for similar CAR-T cell experiment which revealed statistical significance in previous experiments.

Data exclusions

Yeast display: No data were excluded from the analyses.
 In vitro Stat5 experiments: No data were excluded from the analyses for STAT5 phosphorylation studies and surface plasmon resonance studies. Cell populations were identified based on forward/side scatter profiles and singlets were discriminated using forward scatter area versus height plots.
 Ex vivo Stat5 experiments: No data were excluded from the analyses.
 In vivo Airway inflammation experiments: Two samples were excluded from analysis of % lung resident CD8+ T cells in Figure 4b due to failure of intravascular labeling (Thy1.2-BUV395) prior to sacrifice, as determined by the absence of Thy1.2+ cells in the collected sample.
 Colorectal carcinoma in vivo experiments: No data were excluded from the analysis
 Melanoma in vivo experiments: For melanoma tumor model experiments, no data points were excluded from analysis.
 Car-T cells in vivo experiments: No data were excluded from the analysis

Replication

Yeast display: All experiments were repeated at least once and all attempts of replication were successful.
 In vitro Stat5 experiments: All STAT5 phosphorylation studies were performed in triplicate and iterated at least 3 times to ensure reproducibility. Surface plasmon resonance studies were performed at least twice to ensure reproducibility.
 Ex vivo Stat5 experiments: All experiments were repeated and all attempts of replication were successful.

In vivo Airway inflammation experiments: All experiments were repeated and all attempts of replication were successful.

Colorectal carcinoma in vivo experiments: Experiments were repeated with similar results that are included in the extended information.

Melanoma in vivo experiments: Findings were conserved across a minimum of two experiments.

Car-T cells in vivo experiments: Experiments were not repeated, but multiple subjects were included in each experimental group.

Randomization	Yeast display: Not used.
	In vitro Stat5 experiments: Not used.
	Ex vivo Stat5 experiments: Not used. Mice used in the in vivo experiments were purchased from The Jackson Laboratory and randomly allocated into experimental groups upon receipt.
	In vivo Airway inflammation experiments: Mice used in the in vivo experiments were purchased from The Jackson Laboratory and randomly allocated into experimental groups upon receipt.
	Colorectal carcinoma in vivo experiments: Mice were randomly assigned into each experimental group according to their tumor volumes and in order to attain an even tumor volume average across experimental groups.
	Melanoma in vivo experiments: The mice were given tumors and then randomized after tumor injection to specific treatments. In some instances, mice were further randomized if a treatment was started later in the experiments. This is specifically stated in the methods or figure legend when that was the case.
Blinding	Car-T cells in vivo experiments: Mice were randomly allocated into experimental groups.
	Yeast display: Investigators were not blinded to the treatment groups.
	In vitro Stat5 experiments: Investigators were not blinded to the treatment groups.
	Ex vivo Stat5 experiments: Investigators were not blinded to the treatment groups.
	In vivo Airway inflammation experiments: Investigators were not blinded to the treatment groups. Blinding was not relevant as mice were not scored throughout treatment.
	Colorectal carcinoma in vivo experiments: Investigators were not blinded to the treatment groups.
	Melanoma in vivo experiments: Investigators were not blinded to the treatment groups.
	Car-T cells in vivo experiments: Investigators were not blinded to the treatment groups.

Reporting for specific materials, systems and methods

Materials & experimental systems

n/a	Involved in the study
<input type="checkbox"/>	<input checked="" type="checkbox"/> Unique biological materials
<input type="checkbox"/>	<input checked="" type="checkbox"/> Antibodies
<input type="checkbox"/>	<input checked="" type="checkbox"/> Eukaryotic cell lines
<input checked="" type="checkbox"/>	<input type="checkbox"/> Palaeontology
<input type="checkbox"/>	<input checked="" type="checkbox"/> Animals and other organisms
<input checked="" type="checkbox"/>	<input type="checkbox"/> Human research participants

Methods

n/a	Involved in the study
<input checked="" type="checkbox"/>	<input type="checkbox"/> ChIP-seq
<input type="checkbox"/>	<input checked="" type="checkbox"/> Flow cytometry
<input checked="" type="checkbox"/>	<input type="checkbox"/> MRI-based neuroimaging

Unique biological materials

Policy information about [availability of materials](#)

Obtaining unique materials

Materials related to this manuscript are available upon request to the corresponding authors.

Antibodies

Antibodies used

Yeast display: FITC-conjugated anti-c-Myc antibody

In vitro Stat5 experiments:

- Alexa Fluor® 647-conjugated mouse anti-STAT5 pY694 (BD Biosciences, 612599, Clone 47/Stat5(pY694))
- AlexaFluor 700 anti-CD44, clone IM7

Ex vivo Stat5 experiments:

- PE anti-pSTAT5 (pY694), clone 47
- PE-Cy7 anti-CD25, clone PC61
- PerCP anti-CD4, clone RM4-5
- AF700 anti-CD44, clone IM7

In vivo Airway inflammation experiments:

- FITC anti-Ki67, clone SolA15
- PerCP-Cy5.5 anti-CD25, clone PC61
- eFluor 450 anti-Foxp3, clone FJK-16S
- BV510 anti-CD8, clone 53-6.7
- BV605 anti-PD-1, clone J43
- BV711 anti-CD4, clone RM4-5
- BV786 anti-CD62L, clone MEL-14
- PE anti-CD69, clone H1.2F3
- PE-CF594 anti-B220, clone RA3-6B2
- PE-Cy7 anti-CXCR5, clone 2G8
- BUV395 anti-Thy1.2, clone 53-2.1

Colorectal carcinoma in vivo experiments: (BioLegend antibodies):

- Brilliant Violet 510™ anti-mouse CD45 Antibody, 103138, 30-F11, B235434;
- Brilliant Violet 711™ anti-mouse CD3 Antibody, 100241, 17A2, B245637;
- FITC anti-mouse CD49b (pan-NK cells) Antibody, 108906, DX5, B159570;
- Brilliant Violet 605™ anti-mouse CD4 Antibody , 100548, RM4-5, B244808;
- PE/Cy7 anti-mouse CD8a Antibody, 100721, 53-6.7, B239089;
- FOXP3 Monoclonal Antibody (FJK-16s), APC, eBioscience™, 17-5773-82, FJK-16s, 4303649.

Melanoma in vivo experiments: (BioLegend antibodies):

- CD45-BV711 (clone 30-F11, catalog 103147, lot number B243834),
- CD8-BV650 (53-6.7, 100742, B249326),
- CD4-BV421 (GK1.5, 100443, B244726),
- TCRβ-BV510 (H57-597, 109233, B245719),
- CD25-AF488 (PC61, 102017, B220118),
- FoxP3-PE (MF-14, 126404, B254089).

Validation

Yeast display: Positive and negative controls of specific-binding (for each of the fluorescent labeled targets) were included in each experiment.

In vitro Stat5 experiments: Antibodies were used at the dilutions recommended by the manufacturer and validated using appropriate positive (cytokine-stimulated cells) and negative (unstimulated cells) controls.

Ex vivo Stat5 experiments: Positive controls of specific-binding (for each of the fluorescent labeled targets) were included in each experiment.

In vivo Airway inflammation experiments: N/A

Colorectal carcinoma in vivo experiments: Every antibody was previously validated by the manufacturer. All antibody stainings were previously titrated and tested by single-staining. Numerous references were cited in the product's web-page.

Melanoma in vivo experiments: antibodies were validated by BioLegend; citations are available on the manufacturer's website.

Eukaryotic cell lines

Policy information about [cell lines](#)

Cell line source(s)

In vitro Stat5 experiments: CRL-2 cells were purchased from ATCC.
 Colorectal carcinoma in vivo experiments: CT26.WT (ATCC® CRL-2638™).
 Melanoma in vivo experiments: B16 cells were obtained from the ATCC.

Authentication

In vitro Stat5 experiments: ATCC provided authentication for cell lines.
 Colorectal carcinoma in vivo experiments: no authentication was performed.

Mycoplasma contamination	Melanoma in vivo experiments: no authentication was performed. In vitro Stat5 experiments: All cells tested negative for mycoplasma contamination via PCR assay. Colorectal carcinoma in vivo experiments: Cell line was tested negative for mycoplasma using the MycoAlert™ Mycoplasma Detection Kit from Lonza. Melanoma in vivo experiments: testing for mycoplasma was done every 3-6 months.
Commonly misidentified lines (See ICLAC register)	None.

Animals and other organisms

Policy information about [studies involving animals; ARRIVE guidelines](#) recommended for reporting animal research

Laboratory animals	Ex vivo Stat5 experiments: Female wild-type C57BL/6J and CD25KO mice aged 6-8 weeks were purchased from The Jackson Laboratory and used in the experiments. In vivo Airway inflammation experiments: Female wild-type C57BL/6J and CD25KO mice aged 6-8 weeks were purchased from The Jackson Laboratory and used in the experiments. Colorectal carcinoma in vivo experiments: Mus musculus, BALB/c, female and male, age between 10-12 weeks of age. Melanoma in vivo experiments: Female C57BL/6 mice between 6 and 8 weeks old were used. Car-T cells in vivo experiments: NSG mice were obtained from the Jackson Laboratory
Wild animals	None
Field-collected samples	None

Flow Cytometry

Plots

Confirm that:

- The axis labels state the marker and fluorochrome used (e.g. CD4-FITC).
- The axis scales are clearly visible. Include numbers along axes only for bottom left plot of group (a 'group' is an analysis of identical markers).
- All plots are contour plots with outliers or pseudocolor plots.
- A numerical value for number of cells or percentage (with statistics) is provided.

Methodology

Sample preparation	Yeast display: Yeast were grown in C-Trp-Ura media prior to induction in SGCAA media as previously described. 12-18 hours after induction, cells were washed in chilled display buffer (50mM NaPO4 pH 8, 20mM NaCl, 0.5% BSA) and incubated with varying concentrations of biotinylated receptor (either human or murine IL-2R α or IL-2R β , γ c) while being agitated at 4°C. After approximately 30 minutes, cells were washed again in chilled buffer, and then incubated on ice for 5 minutes with FITC-conjugated anti-c-Myc antibody (1 μ L per 3x10 ⁶ cells) and streptavidin-phycerythrin (1 μ L per 100 μ L volume of yeast). Yeast were then washed and counted by flow cytometry (Accuri C6) or sorted by FACS (Sony SH800). In-vitro Stat5 experiments: Cells were stimulated for 15 min at 37°C and immediately fixed by addition of formaldehyde to 1.5% and 10 min incubation at room temperature. Permeabilization of cells was achieved by resuspension in ice-cold 100% methanol for 30 min at 4°C. Fixed and permeabilized cells were washed twice with FACS buffer (phosphate-buffered saline [PBS] pH 7.2 containing 0.1% bovine serum albumin) and incubated with Alexa Fluor® 647-conjugated anti-STAT5 pY694 (BD Biosciences) diluted 1:50 in FACS buffer for 2 hr at room temperature. Cells were then washed twice in FACS buffer and MFI was determined on a CytoFLEX flow cytometer (Beckman-Coulter). Ex vivo Stat5 experiments: Spleens and lymph nodes were harvested from wild-type C57BL/6J or B6;129S4-Il2ratm1Dw (CD25KO) mice purchased from The Jackson Laboratory and made into a single cell suspension in sort buffer (2% Fetal Calf Serum in pH 7.2 phosphate-buffered saline). CD4+ T cells were enriched through negative selection by staining the cell suspension with biotin-conjugated anti-B220, CD8, NK1.1, CD11b, CD11c, Ter119, and CD19 antibodies at 1:100 for 30 min on ice. Following a wash with sort buffer, anti-biotin MicroBeads (Miltenyi Biotec) were added to the cell suspension at 20 μ L per 10 ⁷ total cells and incubated on ice for 20 minutes. Cells were washed, resuspended and negative selection was then performed using EasySep Magnets (STEMCELL Technologies). Approximately 1 x10 ⁵ enriched cells were added to each well of a 96-well plate in RPMI complete medium with 5% FCS with 10-fold serial dilutions of mIL-2, Super-2, or Neoleukin-2/15. Cells were stimulated for 20 min at 37°C in 5% CO ₂ , fixed with 4% PFA and incubated for 30 minutes at 4°C. Following fixation, cells were harvested and washed twice with sort buffer and again fixed in 500 μ L 90% ice-cold methanol in dH ₂ O for 30 min on ice for permeabilization. Cells were washed twice with Perm/Wash Buffer (BD Biosciences) and stained with anti-CD4-PerCP in Perm/Wash buffer (1:300), anti-CD44-Alexa Fluor 700 (1:200), anti-CD25-PE-Cy7 (1:200), and 5 μ L per sample of anti-pSTAT5-PE pY694 for 45 min at room temperature in the dark. Cells were washed with Perm/Wash and re-suspended in sort buffer for analysis on a BD LSR II flow cytometer (BD Biosciences).
--------------------	---

In vivo Airway inflammation experiments: Circulating T cells were intravascularly labeled and tetramer positive cells were enriched from lymph nodes and spleen or lung as previously described (Hondowicz et al., *Immunity*, 2016). Both the column flow-through and bound fractions were saved for flow cytometry analysis. Cells were surface stained and fixed/permeabilized (eBioscience) according to manufacturer's directions prior to intracellular staining for Foxp3 or Ki67. Samples were then analyzed on a BD LSR II.

Colorectal carcinoma in vivo experiments: Mice tumours were minced, digested using a mix of collagenase I, collagenase IV and DNase I for 20 minutes at 37°C. After digestion the samples were passed through a 100μM cell strainer, and resuspended in cold complete DMEM medium. The cell suspensions from the spleens and the inguinal lymph nodes were obtained through the smashing of the tissues against the filter of a 100μM cell strainer.

Melanoma in vivo experiments: Cell suspensions from spleens, tumors, and tumor-draining lymph nodes were washed once with PBS, and the cell pellet was resuspended in 2% inactivated fetal calf serum then stained.

Instrument

Yeast display: Sony SH800, Accuri C6

In-vitro Stat5 experiments: CytoFLEX, Accuri C6

Ex vivo Stat5 experiments: BD LSR II

In vivo Airway inflammation experiments: BD LSR II

Colorectal carcinoma in vivo experiments: BD LSRFortessa™

Melanoma in vivo experiments: special order BD Biosciences LSRFortessa.

Software

Yeast display: CytExpert Software for CytoFLEX and Flowjo

In-vitro Stat5 experiments: CytExpert Software for CytoFLEX and Flowjo

Ex vivo Stat5 experiments: BD FACSDiva was used for flow cytometry sample collection, and FlowJo 9.9.4 was used for analysis of the flow samples.

In vivo Airway inflammation experiments: BD FACSDiva was used for flow cytometry sample collection, and FlowJo 9.9.4 was used for analysis of the flow samples.

Colorectal carcinoma in vivo experiments: BD FACSDiva software™ for data collection, parameterization and compensation; FlowJo, LCC for data analysis

Melanoma in vivo experiments: analysis was performed on Flowjo 10.4.2.

Cell population abundance

Yeast display: No cell sorting was performed for binding screening assays.

In-vitro Stat5 experiments: No cell sorting was performed.

Ex vivo Stat5 experiments: No cell sorting was performed.

In vivo Airway inflammation experiments: No cell sorting was performed.

Colorectal carcinoma in vivo experiments: No cell sorting was performed.

Melanoma in vivo experiments: No cell sorting was performed.

Gating strategy

In-vitro Stat5 experiments: Cell populations were identified based on forward/side scatter profiles and singlets were discriminated using forward scatter area versus height plots. Gating examples are shown in the supplementary information figures.

Ex vivo Stat5 experiments: Gating strategies are shown in the supplementary information figures.

In vivo Airway inflammation experiments: Gating strategies are shown in the supplementary information figures.

Colorectal carcinoma in vivo experiments: FSC and SSC gating was performed in order to specifically select lymphocytes, according to what is defined as the gating strategy for lymphocytes in lymphoid organs (small size, low complexity). Boundaries between positive and negative were defined according to the unstained sample, single stainings and fluorescence minus one controls in order to prevent the selection of unspecific signal, autofluorescence or parasitic fluorescence from other fluorophores. Gating strategies are shown in the supplementary information figures.

Melanoma in vivo experiments: Gating strategies are shown in the supplementary information figures.

Tick this box to confirm that a figure exemplifying the gating strategy is provided in the Supplementary Information.